minerals

MDPI

Article

Pyrometamorphic Rocks in the Molinicos Basin (Betic Cordillera, SE Spain): Insights into the Generation of Cordierite Paralavas

Isabel Abad [1,*], Mario Sánchez-Gómez [1], Matías Reolid [1] and Vicente López Sánchez-Vizcaíno [2]

[1] Departamento de Geología and CEACTierra, Universidad de Jaén, Campus Las Lagunillas s/n, 23071 Jaén, Spain; msgomez@ujaen.es (M.S.-G.), mreolid@ujaen.es (M.R.)

[2] Departamento de Geología and CEACTierra, Campus Científico Tecnológico de Linares, Universidad de Jaén, 23700 Linares, Jaén, Spain; vlopez@ujaen.es

* Correspondence: miabad@ujaen.es

Received: 27 September 2019; Accepted: 26 November 2019; Published: 30 November 2019

Abstract: A singular thermal anomaly occurred in the Molinicos Miocene, lacustrine, intramontane basin (Betic Cordillera). This gave place to vitreous vesicular materials (paralavas) and baked rocks (clinker) inside of a sequence of marly diatomites and limestones. The chemical composition of the paralavas (SiO_2 = 52–57, Al_2O_3 ≈ 20, Fe_2O_3 = 10–20, K_2O + Na_2O < 2.5, CaO < 4.5, and MgO < 1.5, % in weight), which is very different from typical igneous rocks, and their high-T mineralogy (cordierite, sillimanite, anorthite, mullite, and high-T silica polymorphs) suggest that they formed during a pyrometamorphic event. The occurrence of dry intervals in the lacustrine depositional system, the high Total Organic Carbon contents (>4% in weight) of dark clay layers and the existence of tectonic fractures give the right context for a combustion process. Short-term heating favoured the generation of paralavas, clinker and marbles. Thermodynamic modelling constrains the onset of melting at 870–920 °C for <10 MPa at equilibrium conditions. However, the presence of tridymite and/or cristobalite in clinker and paralavas and the compositional variation in both rock types suggests that the temperature at which first melting occurred ranged between 870 °C and 1260 °C due to melt fractionation processes.

Keywords: cordierite; clinker; combustion metamorphism; Molinicos Basin; paralava; melt fractionation; P-T pseudosection; SEM

1. Introduction

Pyrometamorphic rocks are the highest temperature products owing to contact metamorphism induced by either igneous, combustion or lightning processes. Pyrometamorphism is an unusual metamorphic process typically characterized by low pressures and very high temperatures [1]. Whereas maximum temperature conditions resulting from igneous activity are around 1200 °C at 1 kbar, under atmospheric conditions, the subsurface combustion of organic-rich rocks (i.e., carbonaceous sediments and coal) can lead to temperatures up to 1500 °C triggering peculiar pyrometamorphic processes called combustion metamorphism [2].

The most common subsurface fires occur in peat beds [3–5], coal deposits [6–12], dumps from coal mines [13–15], mud volcanoes [16–18] and bituminous sediments [2,19–30]. A particular case of subsurface fires is described in lakes with predominantly diatomitic sedimentation that are desiccated during drought periods [29].

Except in the mud volcanoes, where gas discharge can facilitate ignition [17], occurrence of self-ignition in natural subsurface fires needs tectonic joints that provide both oxygen access and

evacuation of combustion products [22]. At the same time, thermal isolation is necessary to accumulate locally enough heat until an activation threshold is reached [29]. Thus, depth and extension of the fires are commonly restricted to some tens of square metres, limited in addition by the position of the water table. However, much larger areas have been described reaching hundreds of square kilometres [22].

During combustion metamorphism, the sedimentary rocks around the ignition foci are subjected to certain changes in addition to common dehydration, and decarbonation in case $CaCO_3$ is present. Firstly, the rocks are hardened and, later, they become sintered and recrystallised producing a ceramic texture. The colour of the rocks is also progressively changed from yellow to more intense orange and red, due to iron oxidation, and finally even grey and black when reducing conditions are reached. In any case, this intense thermal metamorphism triggers only limited fusion of the sediments. The released melts may flow along fractures but usually undergo fast cooling producing small amounts of glass with particular mineral assemblages and textures similar to those of fine-grained volcanic rocks. These rocks, which show features and parageneses merging with those of igneous rocks, are called paralavas and the associated baked or partially melted sedimentary rocks are denominated clinker e.g., [24,31–34]. According to Cosca and Essene [35] the mineral assemblages produced in paralavas are partly a function of the temperature, degree of partial melting, and oxidation state related to local gas buffers, in addition to the original bulk composition of the sedimentary protolith. Fast heating and subsequent fast cooling cause only incomplete reaction and associated chemical disequilibrium, which contributes to the peculiar mineral composition of these rocks, different to other facies of contact metamorphism [1].

In this study, we document the occurrence of a subsurface combustion area in a sedimentary basin located in South Spain, the Molinicos Basin, which is an upper Miocene lacustrine basin of the Betic Cordillera (Figure 1). This is the first case of pyrometamorphism described in the Betics. With the aim of finding out the particular factors that triggered this process we have carried out field observations, and mineralogical and geochemical analysis in the materials affected by the combustion metamorphism. In addition, P-T pseudosection calculations from the plausible protolith are compared with the observations in order to understand and explain the origin and the temperature evolution of the observed variety of lithologies and its relationships.

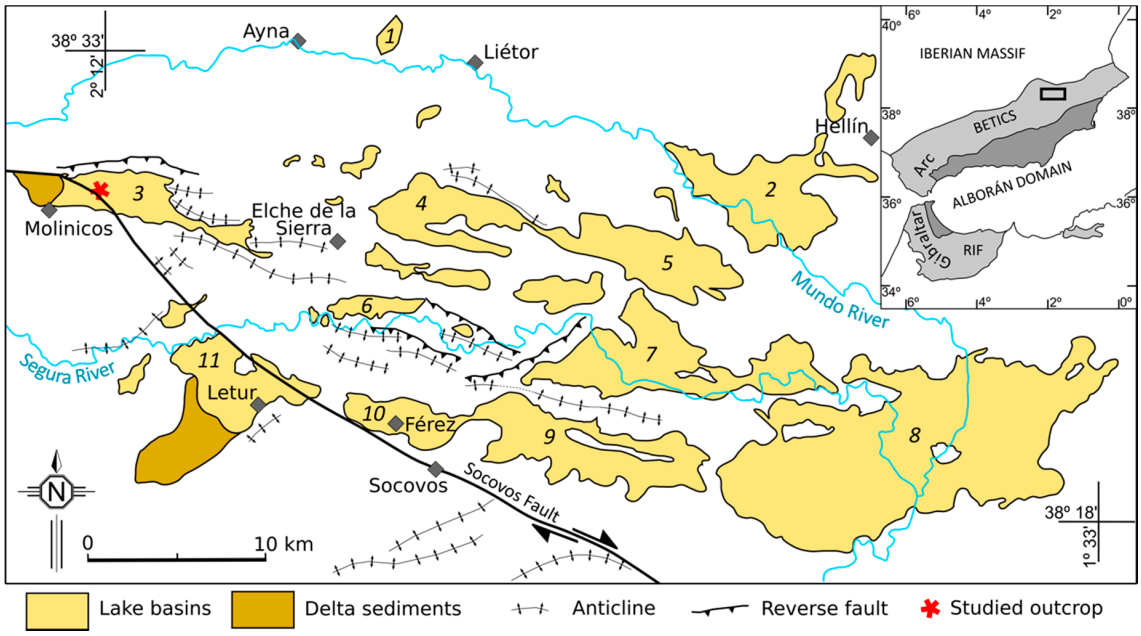

Figure 1. Late Miocene lacustrine basins from the eastern Betics and main related structures. Names of the basins from previous studies e.g., [36–38] and this study: 1, Híjar; 2, Isso; 3, Molinicos; 4, Elche de la Sierra; 5, Cobatillas; 6, Gallego; 7, Cenajo; 8 Las Minas-Camarillas; 9, El Cañar; 10, Férez; 11, Letur. Inset: Location map of the studied area in the SE of the Iberian Peninsula.

2. Geological Setting

The Molinicos Basin forms part of a set of several late Miocene lacustrine basins (Figure 1) that mark out the northeastern limit of the Betic Cordillera [36]. The paleolakes were placed on partially interconnected intramountain basins, which were formed during the tectonic uplift and closure of the so-called North-Betic Strait during the late Tortonian. These basins, ranging from a few km^2 to 250 km^2, formed as rapidly subsiding troughs during the late Vallesian to late Turolian (Tortonian–Messinian of the marine chronostratigraphic scale) [37,39], reaching a thickness of sediments up to 500 m.

The dominant elongation of the basins is ESE–WNW, roughly sub-parallel to the main fault in the vicinity (Figure 1): the Socovos Fault [40,41], a dextral strike-slip fault with lithospheric significance [42]. Basins are located mostly at the north block of the Socovos Fault, and are bounded by anticline ridges (Figure 1). Most of the deformation associated with the fault displacement occurs from early and middle Miocene until Tortonian [41], but continues until nowadays at lower rates [43]. The Molinicos Basin occurs at the western end of the set of lacustrine basins, crossed by the main trace of Socovos Fault (Figure 1). A body of delta conglomerates and sands (≥100 m thick) limits the basin to the west. The observed maximum thickness of lacustrine sediments in this area ranges from 80 to 150 m [37]. According to Foucault et al. [44] and Elizaga [37], the upper Miocene sequence is composed of: (a) conglomerates and sands (turbidites and pelagites), (b) claystones and marly limestones with gypsum, (c) marly limestones and diatomites with organic-rich levels (mainly plant remains), (d) slumped interval, (e) diatomites, limestones and sandy levels (Figure 2).

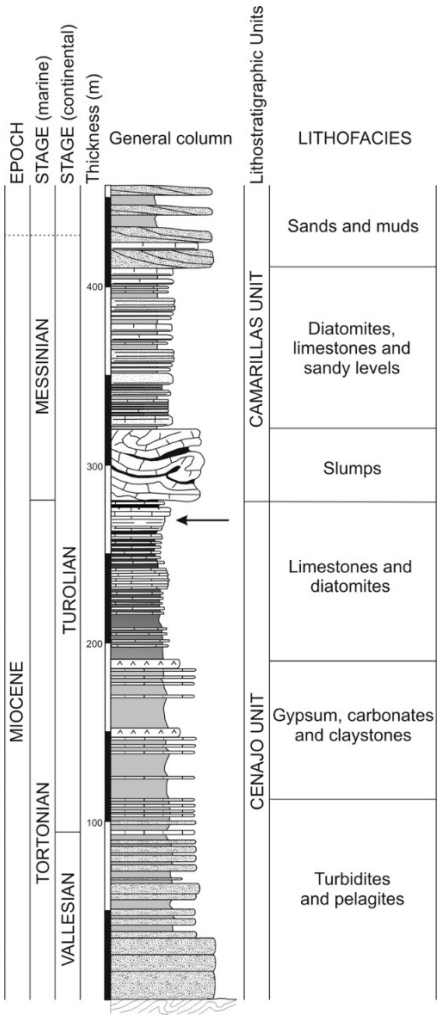

Figure 2. Regional stratigraphic sequence indicating the relative position of the pyrometamorphic site (see black arrow) (modified from Elizaga, [37]).

In the Molinicos Basin, the sedimentary succession is specifically characterized by fine laminated diatomites and limestones (mudstones-wackestones) that can be correlated with the upper Tortonian of the regional sequence. Some limestone beds occur as gastropods- and ostracods-rich wackestones-packstones (Figure 3a) and locally they present fossil mudcracks (Figure 3b). Dark brown to black pelitic layers are found near the pyrometamorphic outcrop separated by a local discordance from the more calcareous sequence on top of them. Organic-rich levels similar to these are described in most of the neighbouring basins [38,45]. Actually, some of these basins have well-known sulphur deposits formed after reduction of sulphates in contact with bituminous lutites or shales [46,47]. The dark levels (10 cm to 30 cm thick, Figure 3c,d) change their thickness in few metres and locally pinch-out. Two main types can be differentiated: (a) dark clay layers resembling black shales and (b) grey clay-rich layers with common vegetal remains, including well-preserved leaves. A metric-sized body of clays crosses through the overlaying beds forming an elongated structure that resembles a mud diapir. Here, the dark clays are oxidized, showing a light ochre colour, and include fragments of surrounding rocks such as green marls. This structure is sub-parallel to the strike of the Socovos Fault (Figure 4).

The pyrometamorphic rocks in the sedimentary succession crop out in a reduced area of 0.4 km^2 crossed by or very close to the estimated Socovos Fault trace (Figure 4).

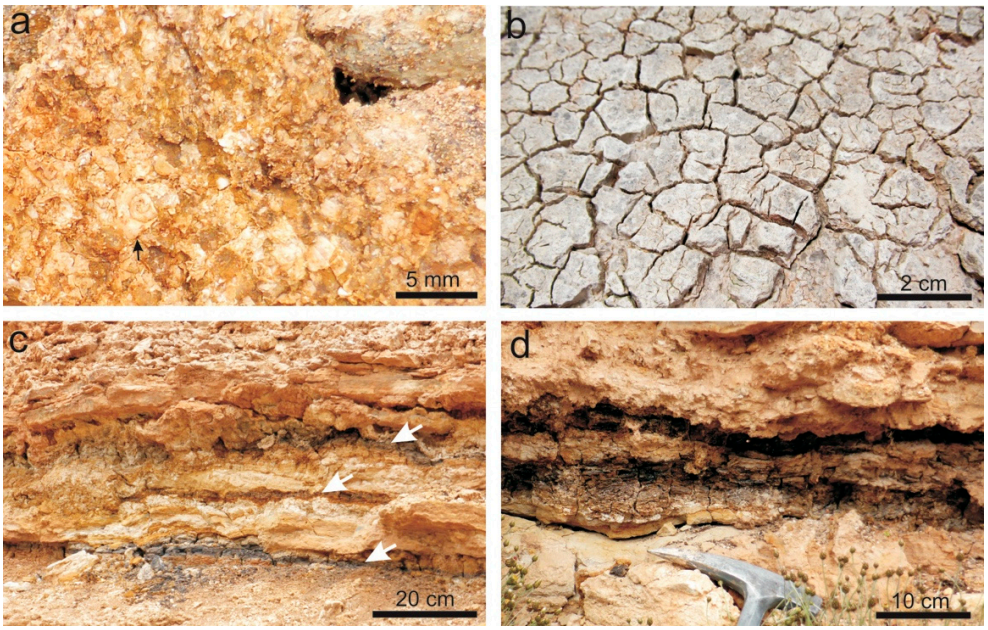

Figure 3. Field pictures from the studied outcrops: (**a**) limestones with gastropods; (**b**) fossil mudcracks and (**c**,**d**) organic-rich clay layers (white arrows in **c**) with calcareous material around.

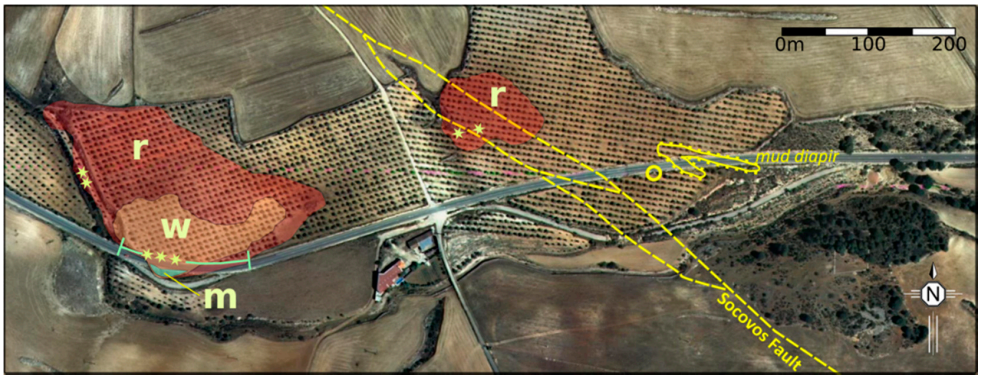

Figure 4. Aerial orthophotomap of the pyrometamorphic outcrop from Molinicos Basin. Location in Figure 1. r: reddish zone (clinker), w: whitened rocks, m: marbles, stars: paralavas, and circle: protolith sample area. Cross section along the road (Figure 5a) is indicated by a segment.

3. Materials and Methods

Fieldwork and mapping allowed us to characterize the distribution and appearance of the studied paralavas and baked rocks. Twenty-seven samples were collected corresponding to: (a) paralavas referring to the massive material relatively mobilized identified in the cross-section of Figure 5a; (b) brick-red rocks forming the clinker which includes fused dark seams; (c) the whitened rocks above the clinker; (d) marbles and (e) rocks obtained from the nearest unaltered sedimentary sequence, which includes dark clay layers and marly diatomites.

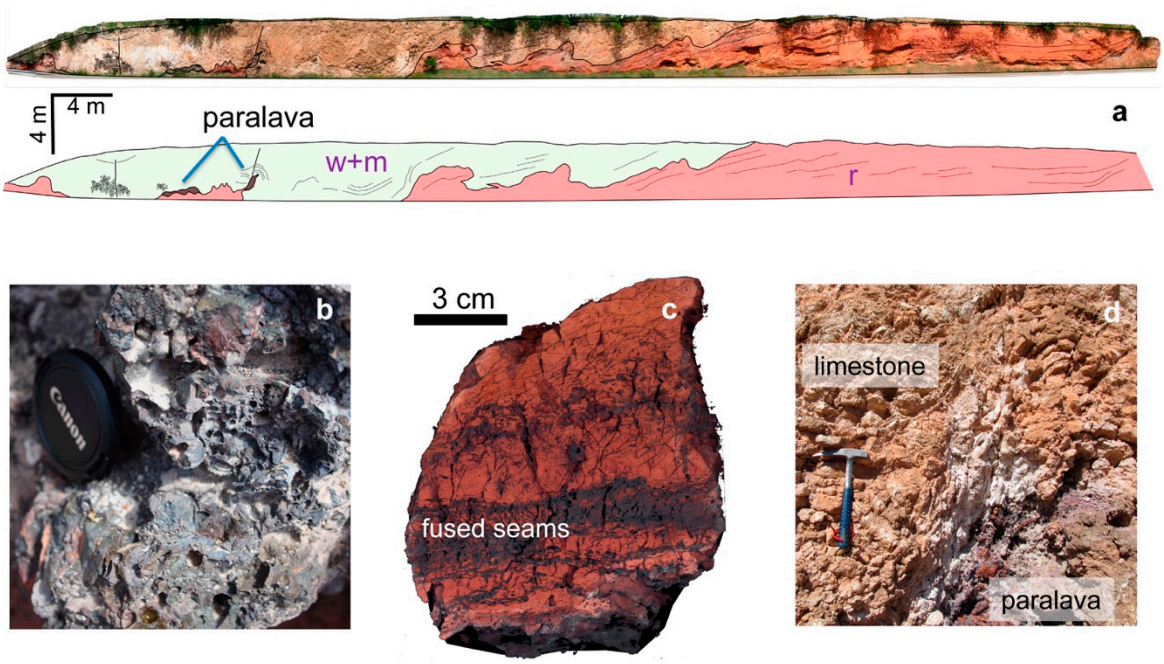

Figure 5. Studied materials: (**a**) Cross-section and field view of the study area with the indication of the different lithologies and structures identified in the outcrop. Location in Figure 4. In pale green, brecciated limestones including laterally undisturbed marbles (w + m) (**c**); in salmon, reddish materials (r, clinker). (**b**) Paralava sample showing a highly vesicular texture. (**c**) Hand sample of reddish materials with incipient fused dark seams. (**d**) Limestone intruded by a paralava.

Whole-rock analyses of the major elements of selected samples from the paralavas, clinker and unaltered rocks were carried out using X-ray fluorescence (XRF) in a Philips Magix Pro (PW-2440) spectrometer and trace elements were analysed using a NexION 300D inductively coupled plasma-mass spectrometer (ICP-MS) (both techniques in the Centro de Instrumentación Científica, CIC, Universidad de Granada, Granada, Spain).

The total organic carbon (TOC) of eight samples corresponding to dark clay layers close to the paralava outcrops was analyzed using a Shimazdu Total Organic Carbon Analyzer (TOC-V sch) from the Instituto de Recursos Naturales y Agrobiología (IRNAS) from CSIC-Sevilla.

X-ray diffraction (XRD) patterns of samples were obtained from powders and oriented aggregates with a PANalytical Empyrean diffractometer equipped with a θ/θ goniometer (Centro de Instrumentación Científico-Técnica, CICT, Universidad de Jaén). The CuK α radiation with a voltage of 45 kV and a current of 40 mA was used with a step size of 0.01° 2θ and a count time of 40 s per step. Samples were scanned from 4° to 64° 2θ. Following the XRD and optical study, carbon-coated polished thin sections were examined by Scanning Electron Microscopy (SEM), using back-scattered electron (BSE) imaging and energy-dispersive X-ray (EDX) analysis to obtain textural and chemical data. These observations were carried out with a Merlin Carl Zeiss SEM (CICT, Universidad de Jaén) and a Zeiss SUPRA40VP, at the CIC of the Universidad de Granada. An accelerating voltage of 20 kV, with a beam current of 1–2 nA and counting time of 30 s were used to analyze the minerals by SEM, using the

following standards: albite (Na), periclase (Mg), wollastonite (Si and Ca), and orthoclase (K), and synthetic Al_2O_3 (Al), Fe_2O_3 (Fe) and $MnTiO_3$ (Ti and Mn). The very small size of some minerals in the studied samples was the reason for the selection of the SEM for the chemical analyses instead of the traditional electron microprobe (EMPA), since the SEM has a higher spatial resolution than the EMPA and the BSE images allow easy selection of very small, contamination-free areas for analyses. WDS analytical data are much more precise (may detect up to 0.02 wt. % of the elements analysed) and if compared to EDX, works under diffraction principles using selected crystals which avoid overlapping elements. In this particular case, EDX analysis of "not overlapping elements" using Na(Kα), Mg(Kα), Al(Kα), Si(Kα), K(Kα), Ca(Kα), Mn(Kα), and Ti(Kα) lines may provide very similar results to the EMPA analysis. In fact, Abad et al. [48] demonstrated that SEM-EDX analyses obtained under the same conditions as EMPA, in particular a careful calibration with real standards and preparation of polished samples, produced equivalent results.

P-T phase-diagram sections (pseudosections) were calculated for bulk-rock compositions of possible suitable protoliths with the aim of estimating their melting conditions and the probable stability conditions of the mineral assemblages observed in the studied clinker and paralava samples. For the same bulk rock compositions, additional, isobaric melt fractionation calculations were made for a heating path, along which a set of incremental temperature steps was determined. After computing the initial stable assemblage for the specified bulk composition, at each temperature increment, the generated, fractionated melt is removed from the system, the system's composition is adjusted and the stable phase assemblage is recalculated.

Calculations were made with Perple_X 6.8.7 [49] in the system $CaO–K_2O–FeO–MgO–Al_2O_3–SiO_2–H_2O$. We used the internally consistent thermodynamic database from Holland and Powell [50,51] and the following solid solution models: clinopyroxene [52]; melt [51,53]; chlorite [54]; olivine, spinel, staurolite, chloritoid, saphirine, garnet [50]; orthopyroxene, biotite [55]; white mica, cordierite [56]; and ternary feldspar [57].

Quartz, tridymite, andalusite and sillimanite were considered as pure phases. Mullite could not be considered in the calculations as it is not included in the employed thermodynamic database of minerals. We used the CORK equation of state for $H_2O–CO_2$ fluids [50], although fluids have been considered pure H_2O. This assumption is consistent with the very low CaO and MgO contents in these rock types (Table 1) and the complete lack of carbonate phases in both clinker and paralava samples (Table 2).

Table 1. Major (wt. %, XRF) and trace element (ppm, ICP-MS) composition corresponding to the paralavas, clinker and potential protolithic materials.

Samples	Clinker		Paralavas			Clay Layer	Marly Diatomite
	CM-17D	**CM-17E**	**CM-17F**	**CM-1**	**CM-13X**	**Y-43**	**Y-81**
SiO_2	58.87	49.79	46.56	56.51	56.77	52.27	26.98
Al_2O_3	26.73	20.22	21.93	20.91	20.32	23.4	8.39
Fe_2O_3*	4.23	18.78	19.8	10.47	11.64	5.44	3.64
MnO	0.02	0.02	0.02	0.43	0.36	0.01	0.02
MgO	1.84	1.09	1.46	1.25	1.26	1.90	1.13
CaO	1.34	2.66	4.33	3.84	3.59	2.91	30.50
Na_2O	0.10	0.30	0.17	0.15	0.12	0.09	0.04
K_2O	2.87	1.92	2.16	1.21	1.23	2.42	0.98
TiO_2	1.24	0.99	1.13	1.15	1.11	1.04	0.44
P_2O_5	0.09	0.25	0.19	1.22	1.20	0.05	0.07
LOI	2.30	3.44	1.75	2.47	1.78	10.29	27.52
TOTAL	99.60	99.46	99.50	99.61	99.38	99.83	99.70

Table 1. *Cont.*

Samples	Clinker			Paralavas		Clay Layer	Marly Diatomite
	CM-17D	CM-17E	CM-17F	CM-1	CM-13X	Y-43	Y-81
Li	34.75	30.64	30.71	44.39	35.80	32.47	12.40
Rb	44.82	61.90	90.37	33.49	68.67	150.63	63.30
Cs	9.11	8.23	8.39	6.38	8.58	12.33	4.34
Be	3.16	3.60	1.87	3.27	3.47	2.65	1.59
Sr	76.45	124.09	142.81	198.58	191.41	85.46	567.77
Ba	195.14	224.98	358.28	522.94	474.19	236.22	146.16
Sc	16.32	13.95	18.98	13.40	13.70	19.81	7.72
V	478.79	700.91	519.69	535.03	523.21	414.29	60.66
Cr	181.97	144.84	199.34	135.76	153.95	146.23	64.78
Co	5.60	7.19	5.84	56.05	48.80	5.89	5.40
Ni	35.47	33.68	37.70	93.78	112.29	26.88	32.74
Cu	50.05	33.39	66.41	39.72	64.08	51.78	14.21
Zn	36.89	47.94	17.25	44.57	75.37	33.42	33.42
Ga	34.60	28.04	7.23	28.42	29.76	34.11	11.90
Y	15.63	27.58	31.68	27.47	28.92	22.00	16.79
Nb	26.36	19.62	25.36	25.34	26.95	19.25	11.01
Ta	2.22	1.62	1.98	1.85	1.75	1.54	0.67
Zr	191.97	133.99	222.62	240.32	214.12	142.77	94.16
Hf	5.52	3.88	6.03	6.72	6.15	3.79	2.07
Mo	64.97	340.81	1113.46	38.79	40.25	415.55	12.49
Sn	4.60	2.71	2.74	0.24	0.47	5.85	2.16
Tl	3.57	3.85	0.29	1.89	3.39	3.27	0.94
Pb	17.47	4.57	0.39	0.36	0.08	30.46	11.68
U	165.86	64.35	200.33	14.58	23.26	4.86	2.57
Th	9.24	12.40	13.34	12.75	13.15	13.21	7.11
La	17.79	36.17	47.37	44.35	47.48	37.87	25.13
Ce	43.90	73.26	100.07	95.45	96.99	85.63	49.04
Pr	5.06	8.60	12.30	11.04	11.31	8.57	5.83
Nd	18.13	31.65	46.05	40.84	41.43	31.20	20.65
Sm	4.56	6.50	9.70	8.44	8.47	6.34	4.35
Eu	1.01	1.39	2.00	1.75	1.71	1.40	0.99
Gd	3.23	5.18	7.59	6.57	6.60	4.64	3.23
Tb	0.59	0.87	1.24	1.08	1.09	0.76	0.54
Dy	3.18	4.55	6.19	5.42	5.45	3.96	2.83
Ho	0.67	0.90	1.11	0.97	0.99	0.77	0.57
Er	1.86	2.27	2.87	2.56	2.55	2.05	1.53
Tm	0.28	0.33	0.41	0.37	0.37	0.31	0.23
Yb	1.80	1.96	2.49	2.29	2.23	1.95	1.45
Lu	0.27	0.29	0.36	0.33	0.32	0.28	0.20

* Total Fe reported as Fe_2O_3. LOI: Loss on ignition.

4. Results

4.1. Field Relationships

Sedimentary rocks affected by pyrometamorphism crop out in two areas (0.008 and 0.045 km^2, respectively), 200 m apart from each other, in the Cerro Morote locality, near the Molinicos village (Figures 1 and 4). The two outcrops might be connected in depth. CM-412 regional road talus revealed a very well exposed cross-section of the pyrometamorphic complex from the largest outcrop (Figure 5a). Two nearly horizontal bodies, with minimum 4 m thickness each, are found along 60 m: the lower one is brick-red in colour (r in Figures 4 and 5) and the upper body is generally whitened and mainly consists of transformed calcareous sedimentary rocks (w in Figures 4 and 5). Both bodies retain much of the original subhorizontal stratification, but locally show a heterogeneous aspect with folds and enhanced fracture networks.

The whitened body is made of fragments of lacustrine limestone beds surrounded by a bright, white, fine-grained matrix in fresh sections. Tabular remains can be recognized, which depict the original bedding through the powder matrix. This matrix is organized or replaced in some places by centimetre thick, concentric layers of calcite. A dark-coloured patina coats the bed remnants in other sectors. Apparently undisturbed beds of lacustrine limestone are found on top of the baked zone at the opposite slope of the road (m in Figure 4). In fresh surface, these rocks show a characteristic bright white colour with black spots typical of marbles, although some gastropod moulds are preserved. Direct continuity between these marbles and the whitened body cannot be observed due to the road digging. However, their common stratigraphic position and proximity (Figure 4) imply that these are two aspects of the same metamorphic body. In this sense, marbles outcrop on the periphery of the pyrometamorphic site.

The reddish body has a layered aspect with alternating yellow to dark ochre bands. It is made mainly of clinker that can be defined here as the red, ochre and black indurated material that maintains part of the sedimentary features. In detail, clinker shows some textural differences that form patches of several metres in length with transitional limits. Massive clinker (sample CM-17D) has spaced non-penetrative fractures and dark colour with lighter reddish patina along joints and layer boundaries. Fresh hammered faces resemble a slate but without cleavage and with millimetric elongated vesicles parallel to the bedding.

Other parts of clinker (sample CM-17E) are made of a dark seam network in a red matrix that gives it a streaky appearance (Figure 5c). Dark seams are of vitreous nature, with a main orientation parallel to the original sedimentary lamination, although its abundance and distribution are heterogeneous on a decimetric scale. Open joints subparallel and oblique to the bedding are penetrative with an average spacing of 10 mm, and connect irregular vesicles up to 20 mm length (Figure 5c). Large areas of the reddish body are made of powdered material that maintain the general aspect defined by the colour alternations, without evidence to discern whether it is a primary alteration (late phases of the pyrometamorphic event) or secondary weathering. The limit between the reddish and whitened domains is irregular and sometimes transitional, in such a way that some limestone beds are included in the reddish body with the surrounding matrix completely coloured.

Two small irregular clusters of dark rocks (<1 × 0.20 m) occur between the reddish and the whitened bodies. According to their position, their mainly vitreous matrix, and the abundance of oval vesicles, occasionally filled, they can be interpreted as paralavas, i.e., almost completely fused rocks (Figure 5b). One cluster lies subhorizontal and resembles a sill, whereas the second one intrudes with vertical orientation following a fracture, and folds the relics of the limestones bedding (Figure 5d). Reddish, partially resorbed, centimetric enclaves resembling the clinker can be observed within both paralava bodies. In turn, volumes of few cubic centimetres of paralavas are spatially related to the dark seams of the clinker inside the reddish body.

4.2. Bulk-Rock Chemical Composition and Total Organic Carbon (TOC) Contents

Whole-rock analyses of the major elements corresponding to paralavas and clinker (Table 1) show high SiO_2 (46.56–58.87 wt. %) and Al_2O_3 (20.32–26.73 wt. %) contents. Total Fe_2O_3 strongly ranges from 4.23 to 19.8 wt.%, although most analysed rocks are above 10 wt. %. No independent analyses of FeO contents were made. However, attending to the observed mineral assemblages (Table 2) and mineral chemistry (Table 3) it can be concluded that hematite is the only abundant Fe-bearing phase in the clinker samples and, thus, most of their Fe content appears as Fe_2O_3. On the contrary, Fe-rich cordierite (with FeO) is abundant in the paralavas (Table 3), which suggests a higher FeO/Fe_2O_3 rate in these rocks. The MgO (<2 wt. %), CaO (<5 wt. %) and total alkalis ($K_2O + Na_2O$ < 3 wt. %) contents are low in every rock type, especially in the case of Na_2O (≤0.3 wt. %).

These compositions (especially those of clinker CM-17D and paralavas CM-1 and CM-13X) compare well with those of the dark clay layers of the nearest sedimentary sequence (sample Y-43; Table 1, Figure 6) and strongly differ from the marly diatomites (sample Y-81), with CaO > 30 wt. %

and low SiO_2 (27 wt. %) (Table 1, Figure 6). Accordingly, it can be suggested that dark clay rocks are the most likely protolith of both clinker and paralavas, at least for the above-mentioned samples. Significant compositional differences between the paralava sample CM-17F and samples CM-1 and CM-13X are also displayed in Figure 6. Compositions of clinker samples CM-17D and CM-17E also differ from each other and can be related to the observed textural differences between them.

The variation of elemental concentrations among dark clay layers (sample Y-43) and clinker and paralava samples (Figure 7) shows a moderate enrichment in Fe_2O_3 and Na_2O, and an impoverishment in volatiles (LOI values), presumably largely H_2O, which decreases from protolith to paralava samples (Table 1). The latter was probably due to the loss of pore water with increasing temperature under low pressure conditions. There is a significant enrichment in MnO, P_2O_5 and U in paralavas (Figure 7b) whereas in the clinker samples this enrichment is only significant in U and moderate in MnO and P_2O_5 (Figure 7a). Apparently, Sn and Pb appear to be decreasing with heating and Sr, Ba, Co, Ni, Zr and Hf increasing with it (Table 1, Figure 7).

Rare earth elements (REE) patterns, normalized to the CI carbonaceous chondrite [58], of protolith, clinker and paralava samples display a common trend with a small negative anomaly in Eu (Figure 8), more evident in the paralavas ($Eu/Eu^*_{protolith}$ = 0.79; $Eu/Eu^*_{clinker}$ = 0.76; $Eu/Eu^*_{paralavas}$ = 0.71). REE concentration in the paralavas is higher than in both the protolith and clinker samples.

TOC contents of dark clay layers recorded close to the paralavas range from 2.8 to 4.0 wt. %. Original values were probably higher since it is known that recent weathering contributes to the TOC loss due to the infiltration of O_2-rich meteoric water [59]. We obtained similar TOC contents (up to 4.6 wt. %) in a slightly fresher outcrop from the nearby Férez Basin (Figure 1).

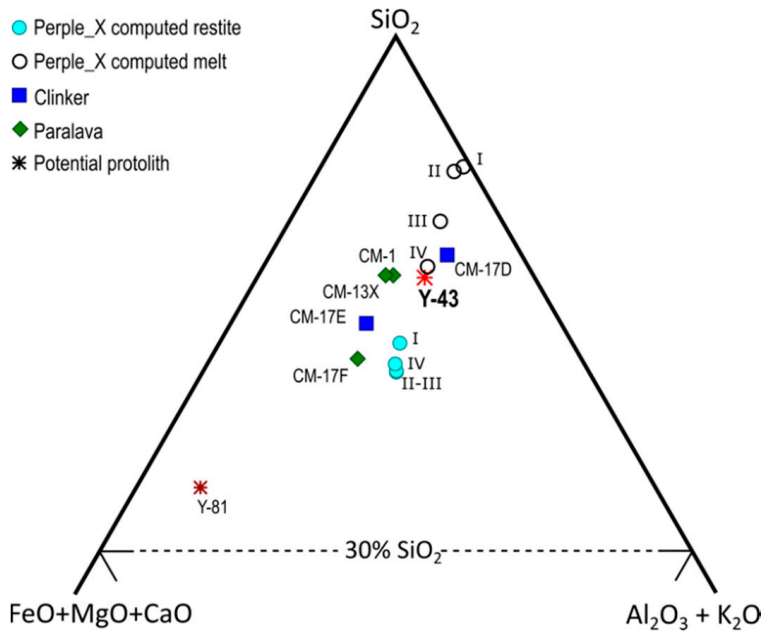

Figure 6. FMAS plot showing the compositions of the studied sediments, clinker and paralava samples (based on XRF data) and those corresponding to the computed melts and restites generated if first melting and fractionation is assumed to happen at temperature conditions of points I to IV in Figure 15b.

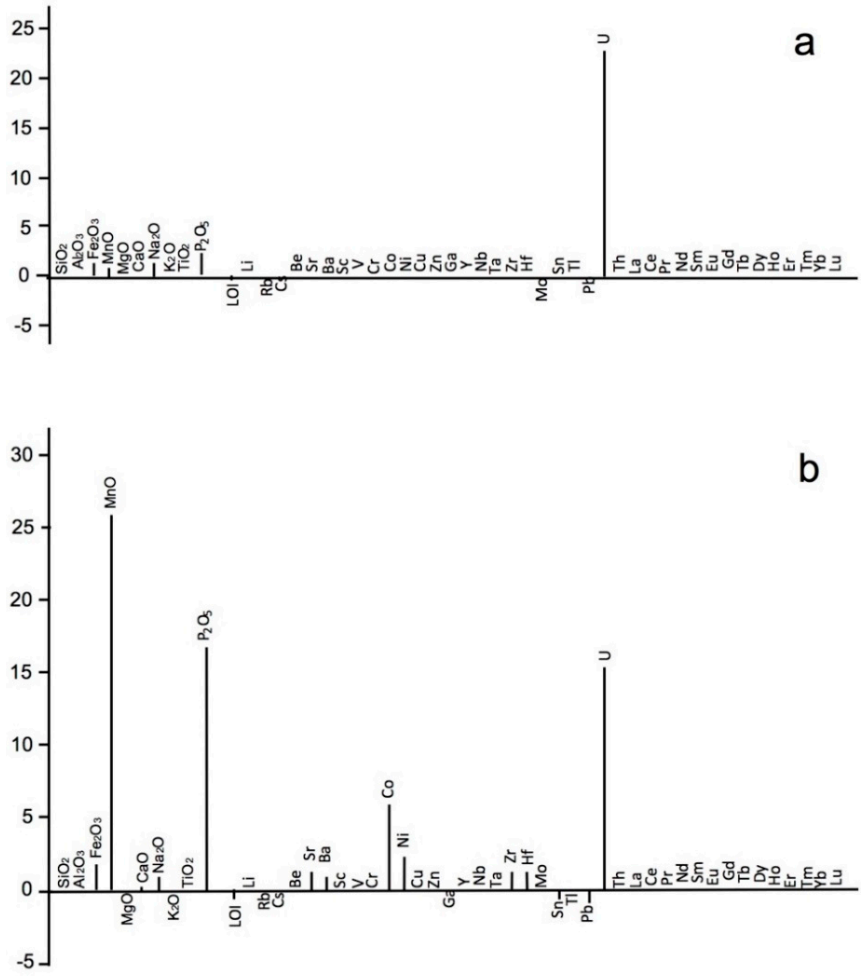

Figure 7. Histograms of mass variation of components in protolith (dark clay layer Y-43) versus components in clinker (**a**) and paralava (**b**) samples. $(M_i^f – M_i^o)/M_i^o$, where M_i^o is the mass of component i in the unaffected rock and M_i^f is the mass of component i in the rocks affected by the pyrometamorphism. The values projected are the average obtained from the two clinker samples (**a**) and the three paralavas (**b**).

Table 2. Mineral assemblages in clinker and paralavas from the Molinicos Basin determined by XRD and SEM.

Minerals	Clinker Samples (r)		Paralava Samples (*)		
	CM-17D	CM-17E	CM-17F	CM-1	CM-13X
Cordierite		X	XX	XXX	XXX
Corundum		X	X		X
Cristobalite		XX		XXX	XX
Feldspars	X	X	XX	XX	X
Hematite	X	XXX	XX		X
Hercynite			X		X
Mullite	XX	X	XX		
Quartz	XX	X		X	X
Sillimanite			XX		X
Tridymite	X	X	X	XX	XX
Zeolites		X	X		

XXX: main phase; XX: moderate; X: scarce.

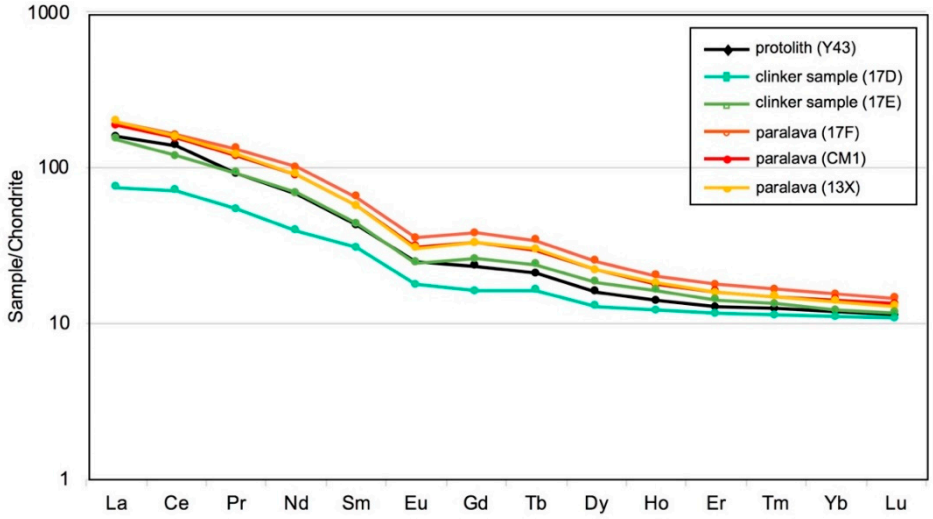

Figure 8. Rare earth elements (REE) patterns, normalized to the CI carbonaceous chondrite [58], for the studied materials.

4.3. Mineralogy (XRD Data and SEM Characterization)

Characterization of the mineral assemblages and textural relationships in the different rock types and in particular, in the clinker and paralavas, were accomplished by XRD and SEM analyses (Table 2 and Figures 9–13).

The so-called dark clay layers, as indicated by the XRD patterns, are mainly composed of quartz, calcite and clays: illite, chlorite, a smectite phase and kaolinite. Some feldspars are also present. The background in the X-ray pattern is quite high, probably owing to the presence of organic matter. Green and ochre marls from the mud diapir consist of calcite, quartz and clay minerals (kaolinite, illite and smectite) as well as feldspars and goethite in the reddest domains. The marly diatomites are, however, characterized by the presence of calcite, aragonite and quartz with subsidiary clay minerals (illite, chlorite and kaolinite).

Rocks from the whitened body, both the fine-grained matrix and bed remnants, are composed only by calcite. Matrix surrounding limestones in the reddish body, next to the limit between the two rock bodies, have quartz and illite in addition to calcite and some dolomite. Nevertheless, the clinker from the reddish body shows a markedly different mineral association. It mainly consists of anorthite and some sanidine, silica polymorphs (quartz, tridymite and cristobalite), mullite, some cordierite in one of the studied samples and corundum (Table 2). Ochre domains are very rich in earthy hematite. X-ray diffractograms show a high background probably motivated by the presence of amorphous vitreous material (Figure 9a).

SEM-BSE imaging of clinker reveals a vesicular texture and an extremely fine-grained or glassy matrix (Figure 10). The only identified crystals are small (<10 μm), corroded, detrital quartz grains (Figure 10a,b), Fe-oxides with variable Al and Ti contents and very rare carbonate clasts. The oxides are clustered around the vacuoles forming aggregates of well-shaped rhomboid crystals of μm scale (Figure 10c). Vacuoles (up to several hundred μm in size) display irregular shapes and are mostly filled with glassy material (Figure 10a,b) composed mainly of SiO_2 and minor quantities of Al_2O_3. Zeolites are less frequent (Figure 10a). XRD data indicate the tridymite was present in the two studied clinker samples whereas cristobalite was only found in one of them (Table 2).

Paralavas display a greater mineral diversity. In addition to the minerals present in the clinker, with less abundant mullite, the XRD data show the presence of aluminosilicates like sillimanite and especially abundant cordierite, as well as cristobalite (Table 2 and Figure 9b). Other than hematite, oxides like corundum, hercynite, rutile, todorokite and Ca-birnessite have been detected by SEM.

BSE images of the paralavas show a clearly vesicular texture, like that of volcanic scoria, with a dark aphanitic groundmass, which includes feldspar, silica polymorphs (thin laths of tridymite and

rounded grains of cristobalite), cordierite phenocrysts (Figures 11 and 12) and idiomorphic sillimanite prisms (Figure 13). Cordierite, with idio- to xenomorphic morphology, has a Fe-rich composition in some cases close to the sekaninaite end-member (Table 3). Hematite and corundum are locally abundant and may occur as individual grains or with an inner part rich in Al inside the rhomboidal crystals (Figure 13). Vesicles range in size from several tens of μm to several mm and they change from rounded or ellipsoidal shapes (Figure 12a) to irregular or elongated ones, even defining a fluidal texture (Figure 11a). They may occur as partial to totally infilled amygdules. In some cases, they are rimmed by concentric thin layers of inner beidellitic smectites, and an outer rim of Mn-rich oxide to F-apatite (Figures 11b and 12b, Table 3). Amygdules are also found filled with apatite (Figure 11c) or, as in the clinker samples, with glassy material (Figure 13b) or with zeolites (Figure 13c, Table 3).

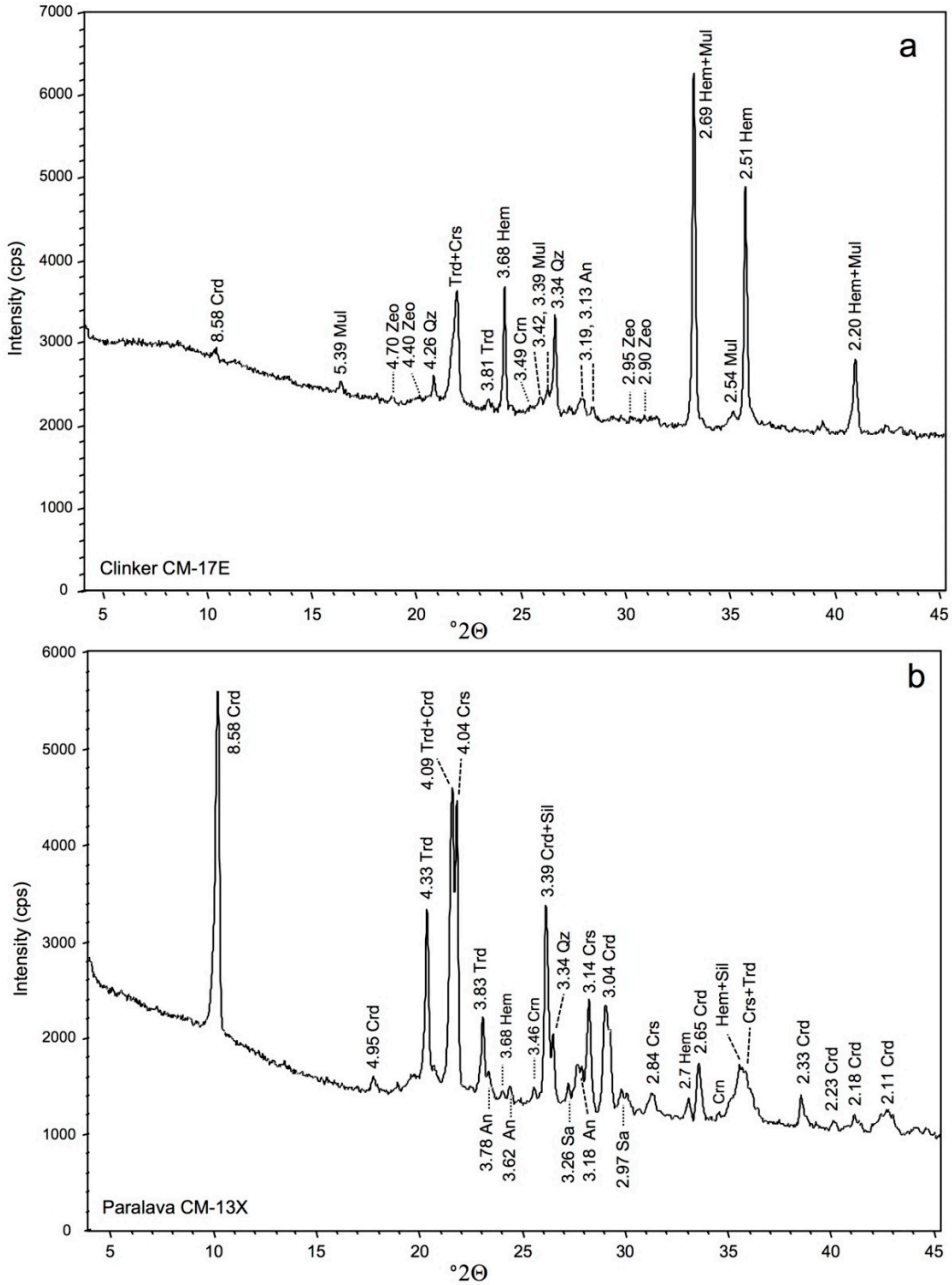

Figure 9. XRD patterns of a clinker sample (**a**) and paralava (**b**). Numbers indicate d values in Å. Note mineral abbreviations according to Whitney and Evans [60]: An, anorthite; Crd, cordierite; Crn, corundum; Crs, cristobalite; Hem, hematite; Qz, quartz; Mul, mullite; Sa, sanidine; Sil, sillimanite; Trd, tridymite.

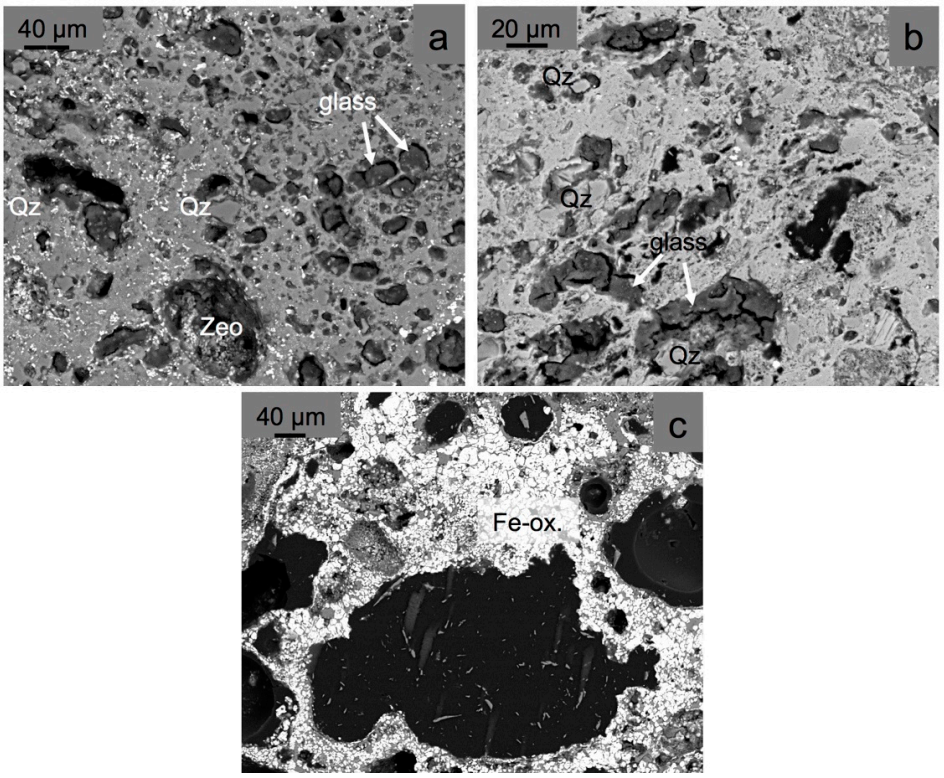

Figure 10. BSE images of clinker: (**a**,**b**) textural aspect of this material with amygdules partial or totally occupied by glass or zeolitic minerals (samples CM-17E and 17D respectively); (**c**) Fe-oxide rich-domains (Fe-ox.) around irregular vacuoles (sample CM-17E). Qz: quartz, Zeo: zeolite.

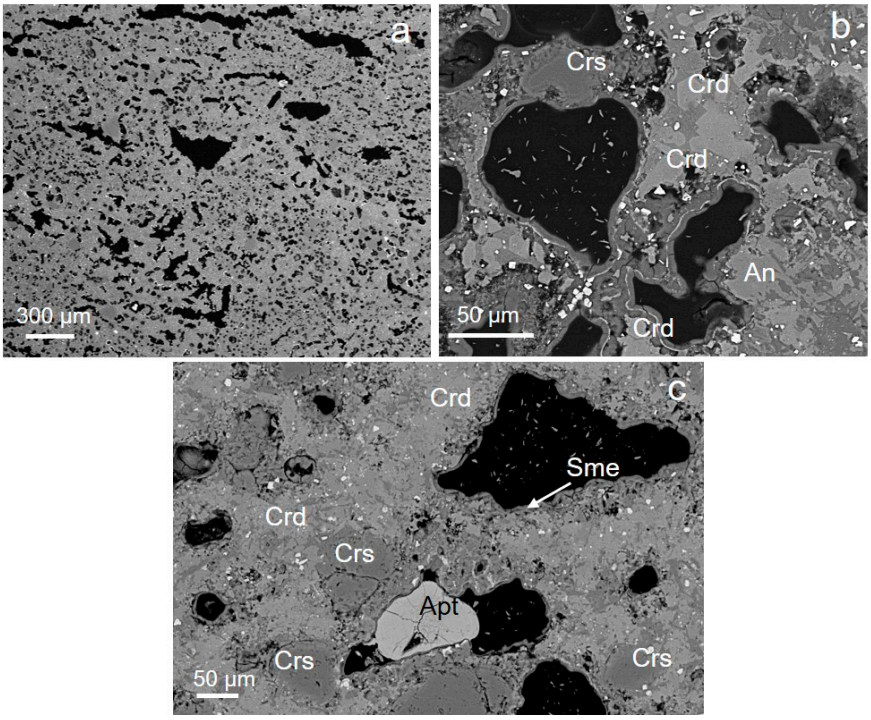

Figure 11. BSE images of paralava CM-13X: (**a**) General view of vesicular texture composed by irregular and coalescing holes; (**b**,**c**) details of the paralava, with mineral characterization of the phenocrysts, mainly cordierite, cristobalite and anorthite immersed in a glassy matrix with irregular vesicles. The lining of the vesicles is similar to the one described in Figure 12b. An: anorthite, Apt: F-apatite, Crd: cordierite, Crs: cristobalite, Sme: smectite.

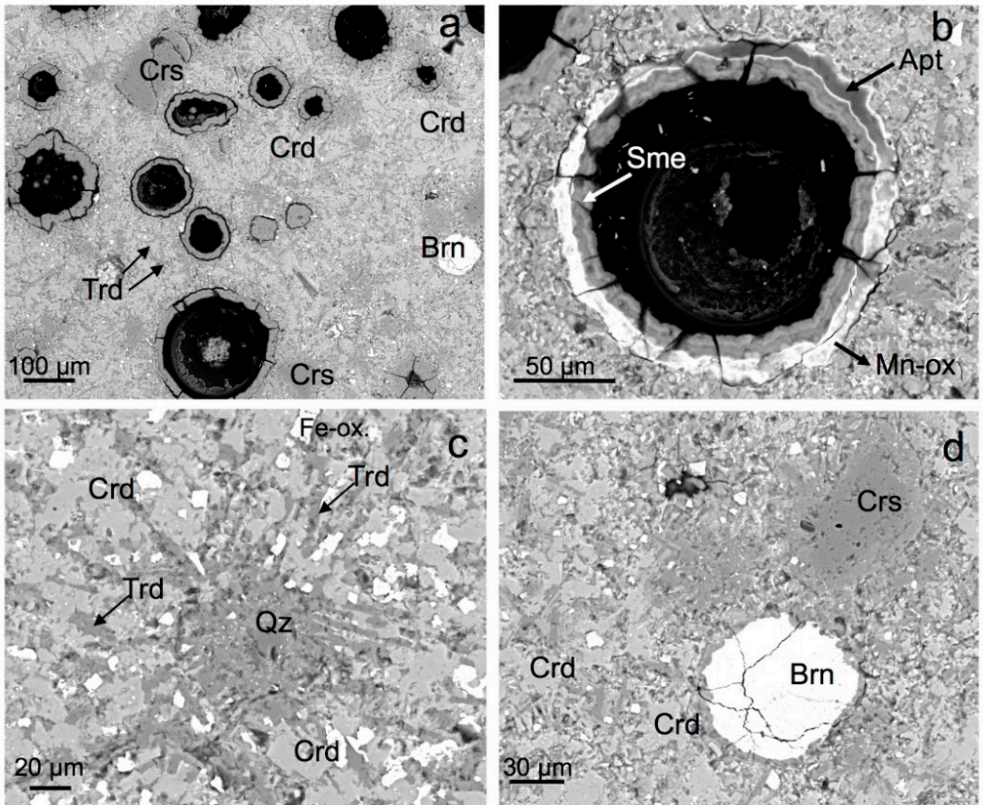

Figure 12. BSE images of paralava CM-1: (**a**) Aphanitic groundmass, which includes very thin laths of tridymite and a vesicular texture characterized by rounded and ellipsoidal coated holes; (**b**) detail of a 20 µm thick vesicle lining formed by a mix of Mn-oxide, F-apatite and beidellitic smectites, the brightest layers correspond to the richest levels in Mn-oxide; (**c**) detail of the paralava showing abundant cordierite and high-T silica polymorphs and Fe oxides; (**d**) detail of (**a**) with a hole entirely occupied by birnessite. Apt: F-apatite, Brn: birnessite, Crd: cordierite, Crs: cristobalite, Mn-ox: oxide of manganese not identified, Qz: silica polymorph, Trd: tridymite.

Table 3. Chemical composition (wt. %) of mineral phases from the Molinicos Basin paralavas and average structural formula calculated.

Analyzed Phases	wt. %										Calculated Average Formula
	Na	Mg	Al	Si	K	Ca	Mn	Ti	Fe	O	
Anorthite	0.1	-	15.3	17.6	0.3	7.5	0.1	0.1	0.3	58.9	$Si_{2.1}Al_{1.9}Ca_{0.9}O_8$
(*n* = 12)	*0.1*	-	*0.7*	*0.7*	*0.2*	*0.6*	*0.0*	*0.0*	*0.1*	*0.6*	
Cordierite	-	2.2	14.6	18.1	0.3	0.1	0.2	0.1	4.9	59.7	$Si_5Al_4(Fe_{1.3}Mg_{0.6}Mn_{0.1})K_{0.1}O_{18}$
(*n* = 21)	-	*0.4*	*1.0*	*1.1*	*0.1*	*0.1*	*0.1*	*0.1*	*0.3*	*2.3*	
Corundum	-	-	38.8	2.1	-	0.0	0.1	0.1	3.1	56.4	$Al_{1.8}Fe_{0.1}Si_{0.1}O_3$
(*n* = 3)	-	-	*2.0*	*1.6*	-	*0.1*	*0.0*	*0.1*	*1.0*	*0.85*	
Hematite	-	0.8	3.3	0.4	*0.0*	0.2	0.7	1.4	39.5	54.2	$Fe_{1.7}Al_{0.2}Ti_{0.1}O_3$
(*n* = 16)	-	*0.6*	*0.8*	*0.4*	*0.0*	*0.2*	*0.8*	*0.7*	*1.9*	*1.9*	
Sillimanite	-	-	25.0	14.1	0.4	0.1	-	0.3	1.0	59.0	$Al_{1.9}Fe_{0.1}Si_{1.0}O_5$
(*n* = 3)	-	-	*1.6*	*2.2*	*0.3*	*0.0*	-	*0.0*	*0.4*	*0.7*	
Silica phases	-	-	0.7	34.2	0.1	0,3	-	0.1	0.24	64.33	SiO_2
(*n* = 18)	-	-	*1.2*	*2.9*	*0.2*	*0.5*	-	*0.1*	*0.33*	*1.36*	
Smectite	-	0.5	13.6	19.4	0.1	0.8	-	0.2	2.4	63.2	$(Si_{3.3}Al_{0.7})(Fe_{0.4}Mg_{0.1}Al_{1.67})Ca_{0.1}O_{10}(OH)_2$
(*n* = 12)	-	*0.2*	*2.4*	*0.8*	*0.0*	*0.2*	-	*0.2*	*1.9*	*0.5*	
Zeolite	-	0.5	11.8	16.1	0.1	0.5	-	0.1	3.4	67.4	$Si_{2.9}Al_{2.1}Fe_{0.6}Mg_{0.1}Ca_{0.1}O_{10}$
(*n* = 4)	-	*0.5*	*12.0*	*16.0*	*0.0*	*0.5*	-	*0.1*	*3.8*	*67.0*	
Vitreous phase	-	-	1.7	33.8	0.2	0.6	-	0.1	0.5	62.9	
(*n* = 14)	-	-	*1.3*	*3.9*	0.2	*0.8*	-	0.1	*0.4*	*4.6*	

Fe as Fe^{2+} in cordierite, sillimanite and zeolite calculations and as Fe^{3+} in oxides and smectite. *n*: number of analyses, standard deviation in italics.

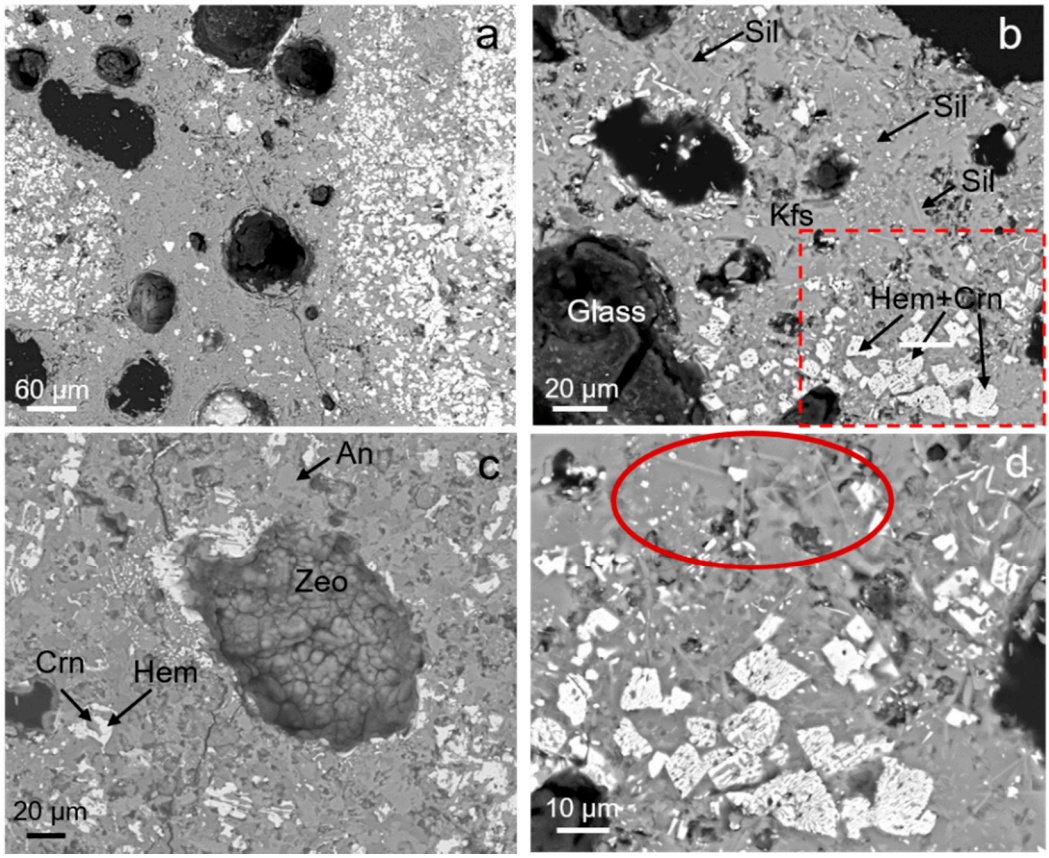

Figure 13. BSE images of paralava CM-17F: (**a**) General view of this sample with a glassy matrix that includes some phenocrysts of anorthite and Fe oxide rich-domains (the ones with the brightest grains); (**b**) Textural aspect of an area with acicular crystals of sillimanite (see also the square sections), feldspars and Fe-Al oxides; (**c**) amygdule filled with a globular aggregate of zeolites; (**d**) detail of (**b**), where, in addition to the oxides, there are many acicular crystals of sillimanite (see the red ellipse zone). An: anorthite, Crn: corundum, Kfs: K-feldspar, Hem: hematite, Sil: sillimanite, Zeo: zeolite.

5. Discussion

5.1. Origin of Pyrometamorphism

The field occurrence, mineral assemblages (Table 2) and textural relationships of the studied rocks (paralavas and clinker), in addition to their atypical bulk composition—with very low alkalis and significant Al_2O_3 and Fe_2O_3 contents (Table 1)—suggest a melting process of sedimentary rocks by subsurface combustion as an explanation for their origin. According to Svensen et al. [29] a spontaneous self-ignition, favoured by exothermal microbial decomposition of organic matter in an environment with good thermal isolation, may cause local accumulation of heat until an activation threshold for burning is reached. In the Molinicos Basin an evolution model can be proposed (Figure 14) that supports a very similar process as the first step for the formation of the here described clinker and paralavas.

The occurrence of dry episodes in the Molinicos lacustrine basin during the Turolian (Late Miocene) (Figure 14b) is evidenced by the record of fossil mudcracks (Figure 3b). During one of these dry episodes the combustion could have occurred as a consequence of subsurface fires promoted by oxidation of organic-rich levels. Actually, the dark clay layers (in black in Figure 14) present a TOC content reaching 4.0 wt. %. These values might have been originally higher (at least 5–16 wt. %) in accordance with TOC contents found in drilling samples from sulfur mining in analogous nearby basins of the same age [38,45]. The syntectonic minor faults and joints related to the Socovos Fault (Figure 14b,c) might

have acted as preferential air flow paths that favoured the penetration of oxygen some metres below the topographic surface, within reach of the burn zone (the organic-rich clay layers), thus supporting the maintenance and propagation of the fire and facilitating the evacuation of the combustion products and smoke.

Combustion of organic matter in the described setting usually involves short-term heating to high temperatures at very shallow depths and subsequent fast cooling promoting the transformation of the protolithic rocks into: (a) paralavas with high temperature mineral assemblages and glass, (b) baked rocks and partially melted (the clinker), and (c) contact metamorphic rocks as the fine-grained marbles described next to the paralavas and clinker (Figure 14c). This kind of thermal alteration is typical of pyrometamorphic processes [1] and has been also reported for the here studied rocks.

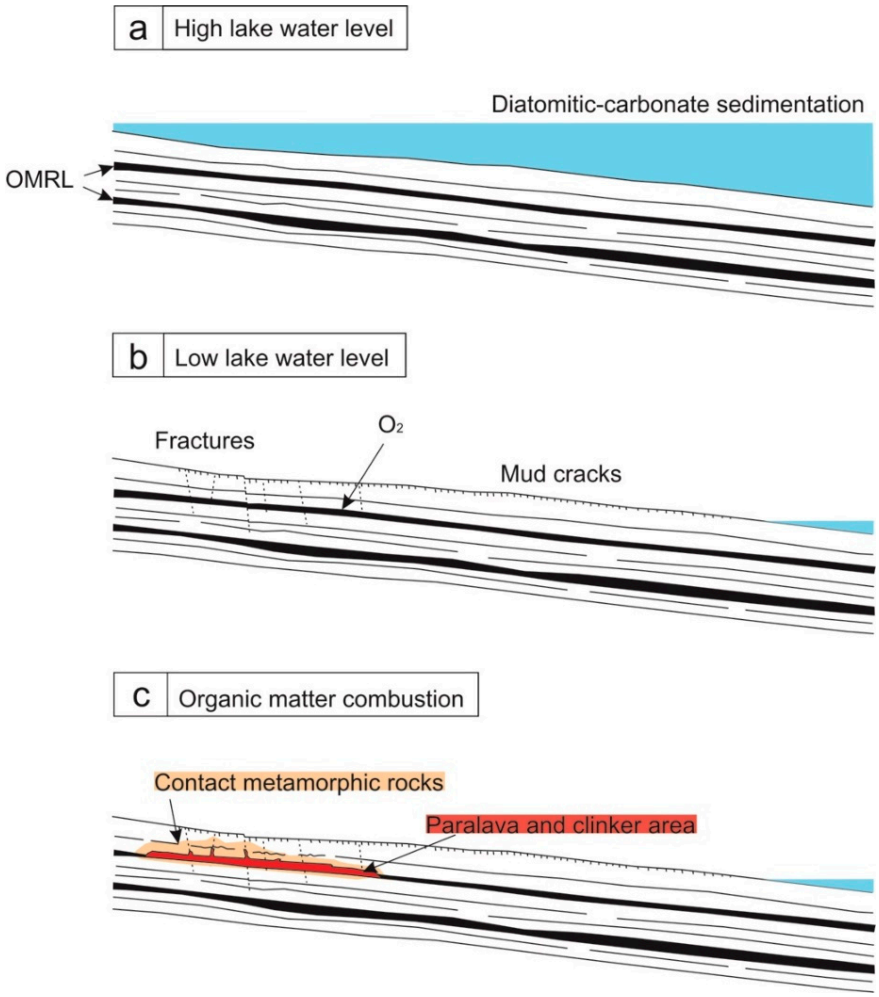

Figure 14. Idealized evolution of the Molinicos lacustrine basin with an upper part of the sedimentary succession characterized by fine laminated diatomites and limestones with intercalations of organic matter rich levels (OMRL). (**a**,**b**) previously to the pyrometamorphic event; (**c**) during the combustion metamorphism. Note: Not to scale.

5.2. Pressure and Temperature Conditions of Pyrometamorphism

Conditions of pyrometamorphism are here estimated by thermodynamic modelling. A P-T pseudosection (Figure 15) has been calculated for the bulk-rock composition of the dark clay layer (sample Y-43; Table 1) since it has a similar composition to that of both clinker and paralavas (Figure 6) and it can be considered as a consistent protolith for these rocks. The very low-pressure range in this diagram (0 to 50 MPa) is consistent with the shallow environment (only few metres depth) that can be deduced from the sedimentary or early diagenetic context of the protolith rock. The observed main

assemblage in the paralavas (cordierite-sanidine-anorthite-sillimanite-tridymite; Table 2) is only stable for the very low-pressure range of 0 to 10 MPa at temperatures of 870 °C to 920 °C, very close to the onset of melting conditions (Figure 15a). According to the phase-diagram, with increasing temperature and melting amounts, sanidine, sillimanite, tridymite, anorthite, and cordierite progressively disappear and at temperatures >1260 °C the rock is completely molten (Figure 15a,b).

This pseudosection, nevertheless, fails to reproduce: (i) the almost lack of cordierite in the clinker samples, (ii) the observed occurrence of coexisting tridymite and cristobalite in both clinker and paralavas and (iii) the reported stability of corundum, hematite, and hercynite (Table 2). These three questions will be addressed below.

In the case of clinker samples, they clearly correspond to rocks that underwent the combined effect of metastable partial melting and quenching of melts (evidenced by the reported dark seams crosscutting them) under chemical disequilibrium conditions [1,61], which makes thermodynamic modelling an apparently meaningless task. However, at temperatures above 900 °C (and especially above 1050 °C) there is a sharp inverse correlation between the modal abundance of cordierite and melt (Figure 15b). Thus, for clinker rocks beyond these temperature conditions, cordierite would have mainly melted and their components incorporated into the present vitreous seams explaining why clinker has a very scarce presence of this mineral.

5.3. Tridymite and Cristobalite Stability

Quartz, tridymite and cristobalite are common minerals in most of the studied rock samples. According to our calculations, transition from quartz to tridymite stability happens at 887 °C and the latter mineral remains stable only up to 970 °C due to melting progression (Figure 15a,b). Independent calculations superposed on the pseudosection (dashed line in Figure 15a) show that cristobalite is only stable at temperatures >1400 °C at $P < 10$ MPa. However, at temperatures >1260 °C the modelled rock is predicted to be completely molten (Figure 15b), thus precluding the preservation of any solid mineral grain.

The common occurrence in pyrometamorphic rocks of relic quartz and of tridymite and/or cristobalite at lower temperatures than those predicted by equilibrium thermodynamics were explained by Grapes [1] indicating that experimentally quartz may persist metastable within the tridymite temperature field and, above 1050 °C, it invariably inverts to cristobalite rather than tridymite. However, these experiments would not explain the here reported coexistence of both tridymite and cristobalite.

Our complementary explanation suggests that the onset of melting might have occurred in the studied rocks at temperatures well beyond those predicted by equilibrium thermodynamics (i.e., that shown in the pseudosection; Figure 15a) and this could have been followed by the fractionation of the generated melt from the rock before quenching (see explanations in Section 3). Both processes are consistent with the already discussed geological setting of the studied pyrometamorphism event: burning of sediments at shallow and brittle conditions (c.f. Section 5.1.).

A fractionation model is shown in Figure 15c for the same bulk rock composition and temperature range of the previous pseudosection, at constant 5 MPa pressure conditions. Removal from the rock of the generated melt (in red) results in wider stability conditions for most minerals (cordierite, feldspar, sillimanite and tridymite) towards higher temperatures. In the tridymite case, it remains stable in the rock without melting up to 1140 °C (blue line in Figure 15c), in contrast with the much lower temperatures (980 °C) of the non-fractionated model (blue line in Figure 15b). Occurrence of stable tridymite in the reported rocks (Table 2) is thus compatible with melt generation at up to 250 °C higher temperatures than those corresponding to first melting conditions. This model, nevertheless, still fails in explaining the reported occurrence of cristobalite, not stable in this diagram (Figure 15c).

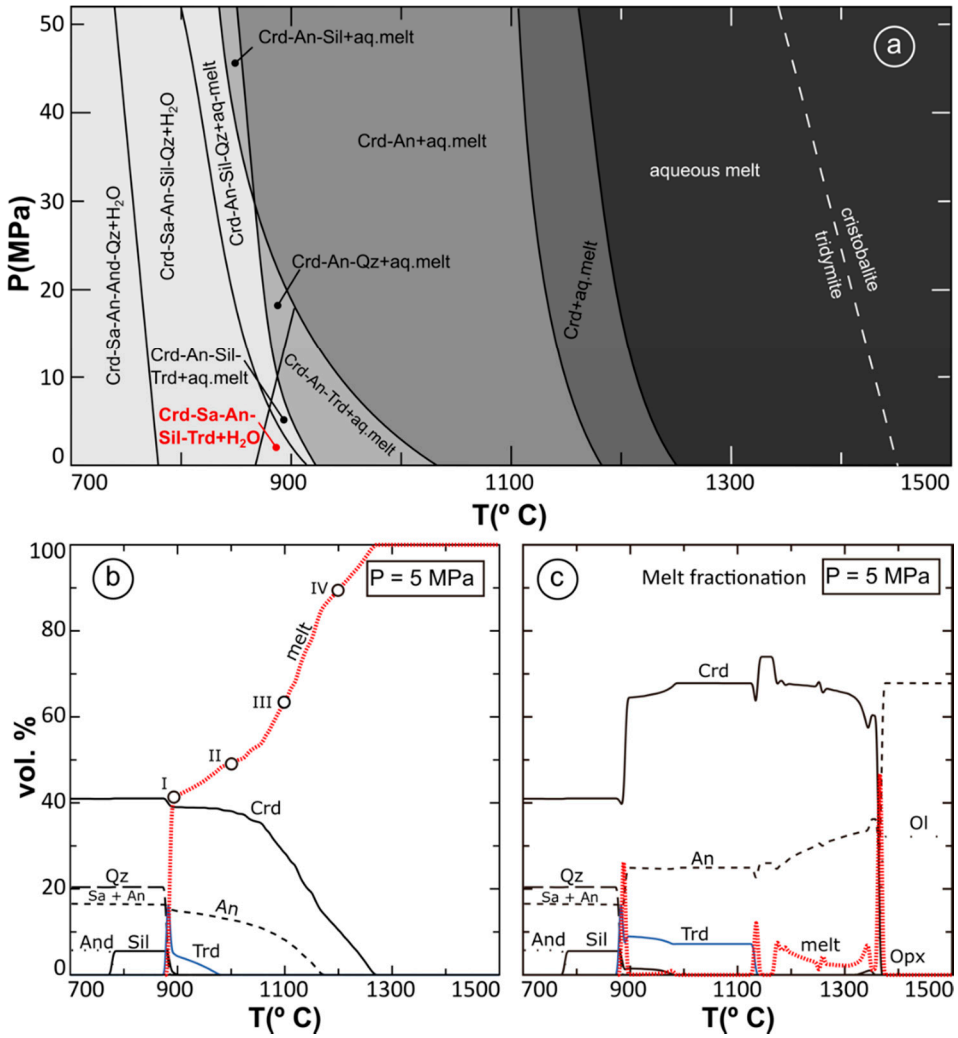

Figure 15. (**a**) P-T pseudosection calculated for the bulk-rock composition of dark clay layer sample Y-43 (Table 1). The bold red label corresponds to the mineral assemblage observed in some rocks (Table 2). The stability conditions for coexisting tridymite and cristobalite are shown by the dashed line at high temperatures. It was independently calculated with Perple_X [49] and superposed onto the pseudosection. (**b**) Isobaric (P = 5 MPa) modal change (as vol. %) of stable minerals and melt in the pseudosection from Figure 15a with increasing temperature. Dots I to IV indicate the temperature conditions (887 °C, 1000 °C, 1100 °C, and 1200 °C) at which the composition of a fractionated melt and the corresponding solid restite were computed (Figure 6) under the assumption that onset of first melting happened at each of those conditions. (**c**) Isobaric (P = 5 MPa) modal change (as vol.%) of stable minerals if the generated melt is fractionated from the rock with increasing temperature. The red line shows the amount of melt generated and fractionated at each temperature condition. Abbreviations for mineral names after Whitney and Evans [60].

5.4. Clinker and Paralava Composition: the Role of Melting Conditions and Fractionation

Attending to their field and textural relationships, clinker and paralava rocks behaved in a very different way during pyrometamorphism. The former would represent rocks in which melting rates were low and with an irregular spatial distribution, followed by fast quenching that gave place to the dark vitreous seams and precluded melt mobilization. Opposite to that, paralavas would essentially represent the concentration of the fractionated melts. However, the fact that the paralavas are scarce and occurring in direct contact with the clinker (Figure 5a) suggests that they only underwent a limited mobilization.

Conditions at which the studied clinker and paralava samples formed can be inferred from the comparison with the melt and restite compositions computed with Perple_X for the fractionation of melt generated at different temperature conditions.

Extreme temperature gradients are typical from pyrometamorphic environments, where temperature may vary by several hundred degrees over a few metres or even centimetres [1]. Accordingly, it can be assumed that the onset of melting, and its first fractionation, could have happened at very different temperatures for the studied rocks. Depending on temperature, the fractionated melt would have a very different composition. In Figure 6 we plotted the modelled melt and restite compositions corresponding to the first melt fractionation at different temperature conditions, as shown by the points labelled I to IV in Figure 15b. As expected, the melts generated at the lowest possible temperatures (I; 887 °C) are very SiO_2-rich whereas if first melting happens at much higher temperatures (IV; 1200 °C) the fractionated melts almost match the protolith bulk composition (dark clay layer Y-43). Restite compositions display a lower variation range but plot along the trend defined by the protolith and melt compositions (Figure 6).

Comparison of this compositional trend with the plotted compositions of the studied clinker and paralava samples is consistent with the following deductions about their formation conditions:

(i) Attending to their very similar composition to dark clays Y-43, the paralavas CM-1 and CM-13X would correspond to a fractionated melt formed at very high temperatures, comprised between 1200–1260 °C, after almost complete melting of their likely clay-rich protolith, similar to sample Y-43. The fact that both paralava samples contain cristobalite (Table 2) indicates that this mineral was stable at lower temperature than those predicted by equilibrium thermodynamics (T > 1400 °C; Figure 15a), as proposed by Grapes ([1]; see above in this section). Additional preservation of other mineral grains, like cordierite, feldspar and tridymite, suggests that total melting was not reached and these minerals were preserved and carried within melt during its presumably short mobilization before quenching.

(ii) Paralava CM-17F has a very different, SiO_2-poorer, composition and could possibly correspond to a different protolith. This would agree with a heterogeneous sedimentary sequence affected by pyrometamorphism. However, an alternative hypothesis would be that this paralava originated after melting at lower temperature conditions than the previous ones. This agrees with the observed occurrence of centimetric-sized clinker enclaves in this sample (with the corresponding lower amount of quenched melt) and the lack of cristobalite in it (Table 2).

(iii) Clinker samples correspond to both restite and non-fractionated rocks. Their wide compositional range (dark blue squares in Figure 6) can be also attributed to different temperatures of onset melting, with the corresponding different melt amount and composition. Thus, the higher SiO_2 content of sample CM-17D indicates that this section of the reddish body reached a lower temperature and produced very limited or not segregated melt, in agreement with the lack of cristobalite in it (Table 2) and the absence of dark seams. On the contrary, sample CM-17E is SiO_2 poorer, but contains stable cristobalite and cordierite (Table 2) which agrees with a higher temperature peak that produces partial melting. Thereby, its restitic composition (Figure 6) can be related with a segregation of melts towards the dark seams, even with migration of material along the penetrative fractures.

5.5. Changes in Effective Bulk Composition and Oxygen Fugacity

The reported extreme temperature gradients typical from pyrometamorphic environments [1] may result in the genesis of diverse high temperature minerals, many of them metastable. The steep temperature gradients can produce burnt to completely melted rocks in a reduced rock volume, thus inducing significant local changes in the effective bulk-rock composition that controls the possible stable mineral assemblages. This might also explain why the observed stability of corundum, hematite, and hercynite (Table 2) could not be reproduced in our pseudosection calculation, in which the initial bulk rock composition was that corresponding to the deduced sedimentary protolith for the studied rocks (dark clay layer Y-43). Sharygin [62] suggests their possible formation due to hot oxidised gases,

as indicated by the accumulation of Fe-Al oxides into, or near, gas vesicles. This could be also the case in the here studied rocks (Figure 13).

In addition, coexistent corundum-hematite pairs can be used for temperature estimations, as shown by Sharygin ([62]; his Figure 9) and references therein, in the case corundum is Fe_2O_3-rich enough. For the here studied samples, mean $Fe^{3+}/(Fe^{3+} + Al)$ mole ratios of coexistent corundum (0.07) and hematite (0.92) (Table 3) would be stable in a 1150–1200 °C temperature range, in good agreement with the above described thermodynamic models.

The characteristic colour of the clinker baked materials owes to the abundant presence of hematite (Figure 10c), higher than in the protolithic samples, usually as the result of the combustion of organic material. According to Cosca et al. [24], the large fO_2 differences over lateral distances of < 2 m promotes differences in the rock oxidation states and also in their colour change from tan to red with increasing oxidizing conditions. XRF bulk analyses (Table 1) show that the iron contents of the clinker reddish rocks and paralavas are rather similar, probably at the expense of the iron oxides produced by the breakdown of the protolith phyllosilicates (mainly illite and smectite).

The combustion process was generally isochemical also for most other major components (Figure 6), except for the dehydration and loss of volatile components. Preferential partitioning of some minor and trace elements in paralavas compared to clinker samples (MnO, P_2O_5, Sr, Ba, Co, Ni, Zr, Hf; Figure 7b) indicates, however, a higher mobility due to melting. This is also the case of REE from Figure 8.

5.6. Cooling Evolution

The secondary minerals lining or filling vesicles (i.e., Mn-oxides, F-apatite and smectites or the globular aggregates of zeolite) in the pyrometamorphic materials suggest subsequent low-temperature, probably hydrothermal, events related to cooling of the rocks. The reported concentric layers of calcite surrounding the limestone relics would confirm this, as well the fluid flow along fractures during cooling. Similar rehydration and zeolitization stages have been also described in equivalent contexts [30,63].

6. Conclusions

In the Molinicos lacustrine basin, subsurface combustion of organic-rich clay layers has triggered partial melting of the sedimentary rocks promoting the genesis of baked rocks (clinker) and paralavas. This is the first pyrometamorphic process identified in the Betics (SE Spain). This event was possible because of the particular characteristics of this sector: a shallow lacustrine basin that dried-up very often and a fractured context due to the proximity of a major active fault that permitted oxygen entrance at depth. Dark clay layers have been identified as the most probable protolith of the pyrometamorphic rocks according to their high TOC contents and bulk-rock composition.

Thermodynamic modelling comprising P-T pseudosections and melt fractionation calculations led to the following comprehensive evolution model of the reported thermal event that explains the observed field and textural relationships in the studied lithotypes:

(1) Main melting started at very low pressures (<10 MPa) and temperatures around 870 °C, at which melt coexisted with the mineral assemblage cordierite-sanidine-anorthite-sillimanite-tridymite that characterizes the paralavas. Nevertheless, due to short-term heating and extreme temperature gradients, the onset of first melting might have occurred in the range comprised between 870 °C and 1260 °C. Depending on temperature, the composition of fractionated melt would be different. This explains the compositional differences observed in both clinker and paralava samples.

(2) The common occurrence of tridymite in most of the studied rocks is compatible with simultaneous melting, at temperatures up to 1140 °C, if a melt fractionation model is considered. However, in spite of thermodynamic predictions, cristobalite was stable in these rocks at temperatures below 1260 °C.

(3) During the combustion, the increase of the oxygen fugacity produced an "out of sequence" mineralogy (corundum, hematite and hercynite) that was not predicted by thermodynamic modelling.

Iron from the breakdown of the sedimentary clays produced ubiquitous hematite, which lent the typical reddish colour to the clinker. Thermometric estimations for coexisting corundum-hematite pairs result in a temperature stability range of 1150–1200 °C, in good agreement with thermodynamic models.

(4) Only a small volume of the overlapping carbonates was affected by the heat increase. Undisturbed limestone beds are turned into very fine-grained marbles, while along fractures networks it is induced the formation of a powdery matrix.

(5) A subsequent cooling hydrothermal stage produced textural alteration and new minerals that filled amygdules in the paralavas and clinker.

Author Contributions: M.S.-G. and M.R. conducted field observations and sampling. I.A. performed microscopic observations in petrographic microscope and SEM (mineralogical, textural, and geochemical analyses) and interpreted the X-ray diffractograms and chemical data (XRF and ICP-MS). V.L.S.-V. made the thermodynamic calculations and modelling. All the authors discussed the analytical results and prepared the manuscript and figures.

Funding: This research was funded by research project No. PGC2018-094573-B-I00 from the MCIU-AEI-FEDER, research projects from CEACTierra (UJA) and Research Groups RNM-325, RNM-370, and RNM-374 of the Junta de Andalucía.

Acknowledgments: We thank J.M. Fernández-Soler for the field and laboratory discussion that focused the research over a non-volcanic origin. Technical and human support provided by CICT of Universidad de Jaén (UJA, MINECO, Junta de Andalucía, FEDER) is gratefully acknowledged. The critical reviews and very helpful comments of the academic editor and two anonymous reviewers have notably improved the quality of the article.

Conflicts of Interest: The authors declare no conflict of interest. The funders had no role in the design of the study; in the collection, analyses, or interpretation of data; in the writing of the manuscript, or in the decision to publish the results.

References

1. Grapes, R. *Pyrometamorphism*; Springer: Berlin, Germany, 2011; p. 365.
2. Sokol, E.V.; Volkova, N.I. Combustion metamorphic events resulting from natural coal fires. In *GSA Reviews in Engineering Geology XVIII: Geology of Coal Fires: Case Studies from Around the World*; Stracher, G.B., Ed.; Geological Society of America: Boulder, GO, USA, 2007; pp. 97–115.
3. Moreno, L.; Jiménez, M.E.; Aguilera, H.; Jiménez, P.; de la Losa, A. The 2009 Smouldering Peat Fire in Las Tablas de Daimiel National Park (Spain). *Fire Technol.* **2011**, *47*, 519–538. [CrossRef]
4. Rein, G. Smoldering-Peat Megafires: The Largest Fires on Earth. In *Coal and Peat Fires: A Global Perspective*; Stracher, G.B., Prakash, A., Sokol, E.V., Eds.; Elsevier Inc.: Amsterdam, The Netherlands, 2015; Volume 4, pp. 1–11. [CrossRef]
5. Prat-Guitart, N.; Nugent, C.; Mullen, E.; Mitchell, F.J.G.; Hawthorne, D.; Belcher, C.M.; Yearsley, J.M. History of irish peatland fires. In *Coal and Peat Fires: A Global Perspective*; Stracher, G.B., Prakash, A., Sokol, E.V., Eds.; Elsevier Inc.: Amsterdam, The Netherlands, 2019; Volume 5, pp. 452–482. [CrossRef]
6. Akulov, N.I.; Akulova, V.V.; Khudogonova, E.V. Pyrogenic metamorphism of the carbonaceous rocks in the south of the Siberian platform. In *Coal Combustion Research*; Grace, C.T., Ed.; Nova Science Publishers: Hauppauge, NY, USA, 2011; pp. 219–234.
7. Kim, A.G. Coal Formation and the Origin of Coal Fires. In *Coal and Peat Fires: A Global Perspective*; Stracher, G.B., Prakash, A., Sokol, E.V., Eds.; Elsevier: Amsterdam, The Netherlands, 2011; Volume 1, pp. 1–28. [CrossRef]
8. Day, S.; Bainbridge, N.; Carras, J.; Lilley, W.; Roberts, C.; Saghafi, A.; Williams, D. Spontaneous Combustion in Open-Cut Coal Mines: Australian Experience and Research. In *Coal and Peat Fires: A Global Perspective*; Stracher, G.B., Prakash, A., Sokol, E.V., Eds.; Elsevier Inc.: Amsterdam, The Netherlands, 2015; Volume 3, pp. 2–36. [CrossRef]
9. Nolter, M.A.; Aurand, H.W.; Vice, D.H. Anthracite Coal-Mine Fires of Northeastern Pennsylvania. In *Coal and Peat Fires: A Global Perspective*; Stracher, G.B., Prakash, A., Sokol, E.V., Eds.; Elsevier Inc.: Amsterdam, The Netherlands, 2015; Volume 3, pp. 652–665. [CrossRef]

10. Novikova, S.A.; Sokol, E.V.; Novikov, I.S.; Travin, A.V. Ancient Coal Fires on the Southwestern Periphery of the Kuznetsk Basin, West Siberia, Russia: Geology and Geochronology. In *Coal and Peat Fires: A Global Perspective*; Stracher, G.B., Prakash, A., Sokol, E.V., Eds.; Elsevier Inc.: Amsterdam, The Netherlands, 2015; Volume 3, pp. 510–541. [CrossRef]
11. Vice, D.H.; Stracher, G.B.; Eckert, A. Coal Fires of the Pacific Northwest, USA. In *Coal and Peat Fires: A Global Perspective*; Stracher, G.B., Prakash, A., Sokol, E.V., Eds.; Elsevier Inc.: Amsterdam, The Netherlands, 2015; Volume 3, pp. 671–680. [CrossRef]
12. Sharygin, V.V.; Sokol, E.V.; Belakovsky, D.I. Mineralogy and Origin of Fayalite-Sekaninaite Paralava: Ravat Coal Fire, Central Tajikistan. In *Coal and Peat Fires: A Global Perspective*; Stracher, G.B., Prakash, A., Sokol, E.V., Eds.; Elsevier Inc.: Amsterdam, The Netherlands, 2015; Volume 3, pp. 582–607. [CrossRef]
13. Ciesielczuk, J. Coal Mining and Combustion in the Coal Waste Dumps of Poland. In *Coal and Peat Fires: A Global Perspective*; Stracher, G.B., Prakash, A., Sokol, E.V., Eds.; Elsevier Inc.: Amsterdam, The Netherlands, 2015; Volume 3, pp. 464–473. [CrossRef]
14. Misz-Kennan, M.; Tabor, A. The Thermal History of Select Coal-Waste Dumps in the Upper Silesian Coal Basin, Poland. In *Coal and Peat Fires: A Global Perspective*; Stracher, G.B., Prakash, A., Sokol, E.V., Eds.; Elsevier Inc.: Amsterdam, The Netherlands, 2015; Volume 3, pp. 432–462. [CrossRef]
15. Ribeiro, J.; Ania, C.O.; Suárez-Ruiz, I.; Flores, D. The spontaneous combustion of coal-mine waste and stream effects in the El Bierzo Coalfield, Spain. In *Coal and Peat Fires: A Global Perspective*; Stracher, G.B., Prakash, A., Sokol, E.V., Eds.; Elsevier Science Ltd.: Amsterdam, The Netherlands, 2019; Volume 5, pp. 98–124. [CrossRef]
16. Hovland, M.; Hill, A.; Stokes, D. The structure and geomorphology of the Dashgil mud volcano, Azerbaijan. *Geomorphology* **1997**, *21*, 1–15. [CrossRef]
17. Sokol, E.; Novikov, I.; Zateeva, S.; Vapnik, Y.; Shagam, R.; Kozmenko, O. Combustion metamorphism in the Nabi Musa dome: New implications for a mud volcanic origin of the Mottled Zone, Dead Sea area. *Basin Res.* **2010**, *22*, 414–438. [CrossRef]
18. Vapnik, Y.; Khesin, B.; Itkis, S. Geophysical Studies of Pyrometamorphic and Hydrothermal Rocks of the Nabi Musa Mottled Zone, Vicinity of the Dead Sea Transform, Israel. In *Coal and Peat Fires: A Global Perspective*; Stracher, G.B., Prakash, A., Sokol, E.V., Eds.; Elsevier Inc.: Amsterdam, The Netherlands, 2015; Volume 3, pp. 318–337. [CrossRef]
19. McLintock, W.F.P. On the metamorphism produced by the combustion of hydrocarbons in the Tertiary sediments of south-west Persia. *Mineral. Mag.* **1932**, *23*, 207–227. [CrossRef]
20. Levorsen, A.I. *Geology of Petroleum*; W.H. Freeman: San Francisco, CA, USA, 1954; p. 703.
21. Basi, M.A.; Jassim, S.Z. Baked and fused Miocene sediments from the Injana area, Hemrin South, Iraq. *J. Geol. Soc. Iraq* **1974**, *7*, 1–14.
22. Bentor, Y.K.; Kastner, M.; Perlman, I.; Yelin, Y. Combustion metamorphism of bituminous sediments and the formation of melts of granitic and sedimentary composition. *Geochim. Cosmochim. Acta* **1981**, *45*, 2229–2255. [CrossRef]
23. Mathews, W.H.; Bustin, R.M. Why do the Smoking Hills smoke? *Can. J. Earth Sci.* **1984**, *21*, 737–742. [CrossRef]
24. Cosca, M.A.; Essene, E.J.; Geissman, J.W.; Simmons, W.B.; Coates, D.A. Pyrometamorphic rocks associated with naturally burned coal beds, Powder River Basin, Wyoming. *Am. Mineral.* **1989**, *74*, 85–100.
25. Eichhubl, P.; Aydin, A.; Lore, J. Opening-mode fracture in siliceous mudstone at high homologous temperature-effect of surface forces. *Geophys. Res. Lett.* **2001**, *28*, 1299–1302. [CrossRef]
26. Lore, J.S.; Eichhubl, P.; Aydin, A. Alteration and fracturing of siliceous mudstone during in situ combustion, Orcutt field, California. *J. Petrol. Sci. Eng.* **2002**, *36*, 169–182. [CrossRef]
27. Eichhubl, P.; Aydin, A. Ductile opening-mode fracture by pore growth and coalescence during combustion alteration of siliceous mudstone. *J. Struct. Geol.* **2003**, *25*, 121–134. [CrossRef]
28. Planke, S.; Svensen, H.; Hovland, M.; Banks, D.A.; Jamtveit, B. Mud and fluid migration in active mud volcanoes in Azerbaijan. *Geo-Mar. Lett.* **2003**, *23*, 258–268. [CrossRef]
29. Svensen, H.; Dysthe, D.G.; Bandlien, E.H.; Sacko, S.; Coulibaly, H.; Planke, S. Subsurface combustion in Mali: Refutation of the active volcanism hypothesis in West Africa. *Geology* **2003**, *31*, 581–584. [CrossRef]
30. Geller, Y.I.; Burg, A.; Halicz, L.; Kolodny, L. System closure during the combustion metamorphic "Mottled Zone" event, Israel. *Chem. Geol.* **2012**, *334*, 25–36. [CrossRef]

31. Clark, B.H.; Peacor, D.R. Pyrometamorphism and partial melting of shales during combustion metamorphism: Mineralogical, textural, and chemical effects. *Contrib. Mineral. Petrol.* **1992**, *112*, 558–568. [CrossRef]
32. Sokol, E.; Volkova, N.; Lepezin, G. Mineralogy of pyrometamorphic rocks associated with naturally burned coal-bearing spoilheaps of the Chelyabinsk coal basin, Russia. *Eur. J. Mineral.* **1998**, *10*, 1003–1014. [CrossRef]
33. Grapes, R.; Zhang, K.; Peng, Z.I. Paralava and clinker products of coal combustion, Yellow River, Shanxi Province, China. *Lithos* **2009**, *113*, 831–843. [CrossRef]
34. Grapes, R.; Korzhova, S.; Sokol, E.; Seryotkin, Y. Paragenesis of unusual Fe-cordierite (sekaninaite)-bearing paralava and clinker from the Kuznetsk coal basin, Siberia, Russia. *Contrib. Mineral. Petrol.* **2011**, *162*, 253–273. [CrossRef]
35. Cosca, M.A.; Essene, J. Paralava chemistry and conditions of formation, Powder River Basin, Wyoming (abstr.). *EOS* **1985**, *66*, 396.
36. Calvo, J.P.; Rodríguez-Pascua, M.A.; Gómez-Gras, D. Sedimentary features indicative of seismogenetic tectonic activity. Las Minas and Cenajo Neogene basins (External Prebetic Zone, SE Spain). *Rev. Soc. Geol. España* **2014**, *27*, 205–221.
37. Elizaga, E. *Análisis de facies sedimentarias y petrología de los depósitos lacustres de edad Neógeno superior de la Zona Prebética, Albacete, España*; Instituto Estudios Albacetenses Serie I Estudios: Albacete, Spain, 1994; Volume 74, p. 216.
38. Ortí, F.; Rosell, L.; Gibert, L.; Moragas, M.; Playà, E.; Inglès, M.; Rouchy, J.M.; Calvo, J.P.; Gimeno, D. Evaporite sedimentation in a tectonically active basin: The lacustrine Las Minas Gypsum unit (Late Tortonian, SE Spain). *Sediment. Geol.* **2014**, *311*, 17–42. [CrossRef]
39. Calvo, J.P.; Elízaga, E. The Cenajo and Las Minas-Camarillas Basins (Miocene), Southeastern Spain. In *A Global Geological Record of Lake Basins*; Gierlowski-Kordesch, E., Kelts, K., Eds.; Cambridge University Press: Cambridge, UK, 1994; pp. 319–324.
40. Jerez Mir, L. Geología de la zona Prebética en la transversal de Elche de la Sierra y sectores adyacentes (provincias de Albacete y Murcia). Ph.D. Thesis, Univ. Granada, Granada, Spain, 1973.
41. Pérez-Valera, L.A.; Sánchez-Gómez, M.; Pérez-Valera, F.; Azor, A.; Villalaín, J.J. Evolución tectónica de la Falla de Socovos desde el Mioceno hasta la actualidad. *Geotemas* **2012**, *13*, 429–432.
42. Pérez-Valera, L.A.; Rosenbaum, G.; Sánchez-Gómez, M.; Azor, A.; Fernández-Soler, J.M.; Pérez-Valera, F.; Vasconcelos, P.M. Vasconcelos. Age distribution of lamproites along the Socovos Fault (southern Spain) and lithospheric scale tearing. *Lithos* **2013**, *180–181*, 252–263. [CrossRef]
43. Sánchez-Gómez, M.; Pérez-Valera, L.A.; Pérez-Valera, F.; Azor, A. Segmentation of the Socovos Fault based on geological data. In *First Iberian Meeting on Active Faults and Paleoseismology*; Insua-Arévalo, J.M., Martín-González, F., Eds.; Instituto Geológico y Minero de España: Guadalajara, Spain, 2010; pp. 137–140.
44. Foucault, A.; Calvo, J.P.; Elizaga, E.; Rouchy, J.M.; Servant-Vildary, S. Place des dépôts lacustres d'âge miocène supérieur de la région de Hellín (province de Albacete, Espagne) dans l'évolution géodynamique des Cordillères Bétiques. *C. R. de l'Académie des Sci. Ser. II* **1987**, *305*, 1163–1166.
45. Permanyer, A.; Ortí, F.; Inglès, M.; Rosell, L.; Salvany, J.M. Contenidos de materia orgánica de formaciones evaporíticas peninsulares. *Geogaceta* **1991**, *10*, 48–52.
46. Reolid, M.; Abad, I.; Selva, A. Elementos Traza y Tierras Raras en el Azufre Rojo de Hellín (Albacete): Interpretación Paleoambiental. *Macla* **2010**, *13*, 181–182.
47. Lindtke, J.; Ziegenbalg, S.B.; Brunner, B.; Rouchy, J.M. Authigenesis of native sulfur and dolomite in a lacustrine evaporitic setting (Hellín Basin, Late Miocene, SE Spain). *Geol. Mag.* **2011**, *148*, 655–669. [CrossRef]
48. Abad, I.; Nieto, F.; Gutiérrez-Alonso, G. Textural and chemical changes in slate-forming phyllosilicates across the external-internal zones transition in the low-grade metamorphic belt of the NW Iberian Variscan Chain. *Swiss Bull. Mineral. Petrol.* **2003**, *83*, 63–80.
49. Connolly, J.A.D. The geodynamic equation of state: What and how. *Geochem. Geophy. Geosy.* **2009**, *10*. [CrossRef]
50. Holland, T.; Powell, R. An internally consistent thermodynamic data set for phases of petrological interest. *J. Metamorph. Geol.* **1998**, *16*, 309–343. [CrossRef]
51. Holland, T.; Powell, R. Calculation of phase relations involving haplogranitic melts using an internally consistent thermodynamic dataset. *J. Petrol.* **2001**, *42*, 673–683. [CrossRef]
52. Holland, T.; Powell, R. Thermodynamics of order-disorder in minerals. 2. Symmetric formalism applied to solid solutions. *Am. Mineral.* **1996**, *81*, 1425–1437. [CrossRef]

53. White, R.W.; Powell, R.; Holland, T. Calculation of partial melting equilibria in the system Na_2O-CaO-K_2O-FeO-MgO-Al_2O-SiO_2-H_2O (NCKFMASH). *J. Metamorph. Geol.* **2001**, *19*, 139–153. [CrossRef]
54. Holland, T.; Baker, J.; Powell, R. Mixing properties and activity-composition relationships of chlorites in the system MgO-FeO-Al_2O_3-SiO_2-H_2O. *Eur. J. Mineral.* **1998**, *10*, 395–406. [CrossRef]
55. Powell, R.; Holland, T. Relating formulations of the thermodynamics of mineral solid solutions: Activity modelling of pyroxenes, amphiboles, and micas. *Am. Mineral.* **1999**, *84*, 1–14. [CrossRef]
56. White, R.W.; Powell, R.; Holland, T.; Johnson, T.E.; Green, E.C.R. New mineral activity–composition relations for thermodynamic calculations in metapelitic systems. *J. Metamorph. Geol.* **2014**, *32*, 261–286. [CrossRef]
57. Fuhrman, M.L.; Lindsley, D.H. Ternary-Feldspar Modeling and Thermometry. *Am. Mineral.* **1988**, *3*, 201–215.
58. McDonough, W.F.; Sun, S.S. The composition of the Earth. *Chem. Geol.* **1995**, *120*, 223–253. [CrossRef]
59. Suan, G.; Rolleau, L.; Mattioli, E.; Suchéras-Marx, B.; Rousselle, B.; Pittet, B.; Vincent, P.; Martin, J.E.; Léna, A.; Spangenberg, J.E.; et al. Palaeoenvironmental significance of Toarcian black shales and event deposits from southern Beaujolais, France. *Geol. Mag.* **2013**, *150*, 728–742. [CrossRef]
60. Whitney, D.L.; Evans, B.W. Abbreviations for names of rock-forming minerals. *Am. Mineral.* **2010**, *95*, 185–187. [CrossRef]
61. Del Moro, S.; Renzulli, A.; Tribandino, M. Pyrometamorphic processes at the magma hydrothermal system interface of active volcanoes: Evidences from Buchite ejecta of Stromboli (Aeolian Islands, Italy). *J. Petrol.* **2011**, *52*, 541–564. [CrossRef]
62. Sharygin, V.V. A hibonite-spinel-corundum-hematite assemblage in plagioclase-clinopyroxene pyrometamorphic rocks, Hatrurim Basin, Israel: Mineral chemistry, genesis and formation temperatures. *Mineral. Mag.* **2019**, *83*, 123–135. [CrossRef]
63. Galuskin, E.V.; Galuskina, I.O.; Gfeller, F.; Krüger, B.; Kusz, J.; Vapnik, Y.; Dulski, M.; Dzierzanowski, P. Silicocarnotite, $Ca_5[(SiO_4)(PO_4)](PO_4)$, a new "old" mineral from the Negev Desert, Israel, and the ternesite–silicocarnotite solid solution: Indicators of high-temperature alteration of pyrometamorphic rocks of the Hatrurim Complex, Southern Levant. *Eur. J. Mineral.* **2016**, *28*, 105–123. [CrossRef]